Physics – Uspekhi **68** (4) 357 – 373 (2025)

REVIEWS OF TOPICAL PROBLEMS

PACS numbers: **61.46. – w**, **68.70. + w**, **81.16. – c**

ON THE 270th ANNIVERSARY OF M.V. LOMONOSOV MOSCOW STATE UNIVERSITY (MSU)

Exotic nanostructures on metal surfaces

S.V. Kolesnikov, A.G. Syromyatnikov, A.M. Saletsky, A.L. Klavsyuk

DOI: https://doi.org/10.3367/UFNe.2024.08.039736

Contents

Abstract. Today, in addition to widely studied nanoobjects, there are a number of less popular, but no less interesting, exotic nanostructures, which occupy an intermediate position in their physicochemical properties. The article considers the following exotic nanostructures formed in bimetallic systems: atomic superlattices, flat dendrites, finger-shaped protrusions, bound nanostructures embedded in the first layer of a substrate, as well as clusters formed under the surface at a depth of several atomic layers. Both experimental methods for obtaining such nanostructures and theoretical approaches to modeling their formation are discussed in detail. The physicochemical properties of exotic nanostructures and possible prospects for their technical application are also discussed.

Keywords: nanostructures, surfaces, superlattices, dendrites, clusters, formations, bimetallic systems

1. Introduction

Over the past decades, the physics of nanostructures has become a separate field of science, interesting from both fundamental and applied points of view. The fundamental achievements of nanostructure physics undoubtedly include the discovery of the quantum Hall effect [1, 2], quantum conductivity [3, 4], massless electron states in graphene [5–8], and much more. From an applied point of view, the physics of nanostructures allows the creation of devices for recording, storing, transmitting, and processing information of a new generation [9–12], and makes it possible to change the physicochemical properties of known materials and obtain new materials with previously unattainable characteristics [13–15]. At present, nanoparticles and nanostructured materials are used in almost all areas of modern life.

Many review articles, monographs, and textbooks are devoted to the latest achievements in the physics of nanostructures [1, 3, 5, 12–17]. As a rule, either compact nanoparticles in a vacuum, in a solution, or on the surface of crystals, or layered nanostructures with layer thicknesses from one atomic layer to hundreds of nanometers are considered. After the discovery of graphene [6–8], two-dimensional nanostructures that can exist in a free state began to be widely studied. In addition to graphene, boron nitride [18, 19], transition metal dichalcogenides [20–22], layered van der Waals structures [23, 24], etc. have gained wide popularity. An equally popular field is the study of one-dimensional nanostructures: nanocontacts [25–27], nanowires, and atomic chains [28–30]. Fullerenes [31], carbon [32, 33], and semiconductor nanotubes [34, 35] deserve special attention. Many studies are devoted to the formation and physicochemical properties of surface alloys [36].

In addition to the widely studied nano-objects listed above, there are several less popular, but no less interesting, nanostructures, which, in their properties, occupy a certain intermediate position among the structures described above. Below, we will call such nanostructures exotic. A striking example of exotic nanostructures is flat dendrites on the surface of crystals [37, 38]. Both in their shape and in their physical properties, they occupy an intermediate position between two-dimensional and one-dimensional nanostructures. In terms of mathematics, this means that a flat dendrite

S.V. Kolesnikov [(1,*)], **A.G. Syromyatnikov** [(1,2,†)], **A.M. Saletsky** [(1)], **A.L. Klavsyuk** [(1,‡)]
[(1)] Lomonosov Moscow State University, Faculty of Physics, Leninskie gory 1, str. 2, 119991 Moscow, Russian Federation
[(2)] Semenov Federal Research Center for Chemical Physics, Russian Academy of Sciences, ul. Kosygina 4, 119991 Moscow, Russian Federation
E-mail: [(*)] kolesnikov@physics.msu.ru, [(†)] ag.syromyatnikov@physics.msu.ru, [(‡)] klavsyuk@physics.msu.ru

Received 19 April 2024, revised 5 June 2024
Uspekhi Fizicheskikh Nauk **195** (4) 377 – 394 (2025)
Translated by V.L. Derbov

can be characterized by a fractal dimension D_f [39, 40], which takes fractional values in the range from 1 to 2. Studying the dependence of physical properties on fractal dimension is an important task, the solution of which can open new horizons for the practical use of nanostructures.

Since it is not possible to discuss all existing exotic nanostructures within the framework of one review article, we will concentrate on nanostructures formed in bimetallic systems. The physicochemical properties of nanostructures are closely related to their shape, which in turn depends on the conditions of nanostructure formation, primarily on temperature. At low temperatures ($T \approx 1$ K), superlattices of individual atoms can form on the surface of metals. Section 2 is devoted to the formation and physical properties of atomic superlattices. When the temperature increases to 100–200 K, flat dendrites can form on the surface of the same metals [41, 42]. The formation and properties of flat dendrites are discussed in Section 3. At a temperature slightly above room temperature ($T \approx 350-400$ K), surface alloys begin to form. Under certain conditions, this can lead to the formation of either finger-like protrusions [43, 44], discussed in Section 4, or bound nanostructures embedded in the first layer of the substrate [45, 46]. The formation and magnetic properties of the latter are discussed in Section 5. Finally, when the temperature is increased to 600 K, the deposited atoms can form small compact clusters under the surface [47–49]. The formation, detection, and physical properties of such clusters are discussed in Section 6.

To date, exotic nanostructures have not been studied so well that we can confidently talk about their technical application. Therefore, we will mainly discuss their fundamental properties. However, in conclusion, we will discuss possible — in our opinion — prospects for the practical application of the listed exotic nanostructures.

2. Superlattices

2.1 Friedel oscillations of electron density on surface of metals

Interactions between adsorbed atoms or molecules on the surface of a solid can be divided into two classes: direct and indirect. Direct interaction occurs due to the direct exchange of electrons between adatoms, while indirect interaction is also due to interaction with the surface. It is worth noting that this division is very arbitrary, since any interaction occurs with the participation of the surface [50].

One example of indirect interactions is the long-range interaction that occurs on the (111) surfaces of noble metals. On such surfaces, there are the surface states discovered by Shockley [51]. Electrons with the energy of the Shockley surface state form an almost free two-dimensional electron gas localized near the upper surface layer [52, 53]. Surface electrons are scattered by defects [54, 55], adsorbents [54, 56–58], and steps [54, 59], giving rise to the emergence of standing electron waves (i.e., redistribution of charge density), which can be detected using a scanning tunneling microscope (STM). Oscillations of charge density around defects can be detected at large distances (about 70 Å) compared to the lattice parameter. Examples of charge density distribution from a Ce atom on an Ag(111) surface and a step on a Cu(111) surface are shown in Fig. 1a and b, respectively. The presence of two atoms or two defects on the surface leads to interference of electron waves from each of them, which is the cause of indirect long-range interaction between atoms [50], atoms and a step, or defects [54–57, 60, 61].

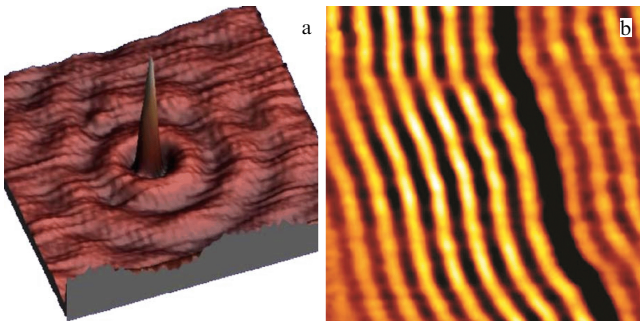

Figure 1. STM image of standing waves of electron density (a) around Ce atom on surface of Ag(111) at a temperature of 4 K [57]; (b) near step of Cu(111) surface at a temperature of 7 K [62].

According to the Bardeen approximation [63], the tunnel current is determined by the expression

$$I = \frac{2\pi e}{\hbar} \sum_{\mu,\nu} f(E_\mu)\left[1 - f(E_\nu + eV)\right] |M_{\mu\nu}|^2 \delta(E_\mu - E_\nu)\,, \quad (1)$$

where $f(E)$ is the Fermi–Dirac function, V is the applied voltage between the STM tip and the surface, $M_{\mu\nu}$ is the transition matrix, and E_μ, E_ν are the energies of an electron in the state μ and ν, respectively. At low temperatures and low voltages, expression (1) takes the form [64]

$$I = \frac{2\pi e}{\hbar}\, e^2 V \sum_{\mu,\nu} f(E_\mu) |M_{\mu\nu}|^2 \delta(E_\mu - E_\mathrm{F}) \delta(E_\nu - E_\mathrm{F})\,. \quad (2)$$

If the STM tip is considered to be a point, then the matrix elements $M_{\mu\nu}$ are proportional to the amplitude ψ_ν at the tip position r_0, and expression (2) is reduced to the form

$$I \propto \sum_{\nu} \left|\psi_\nu(\mathbf{r}_0)\right|^2 \delta(E_\nu - E_\mathrm{F})\,. \quad (3)$$

The quantity on the right in expression (3) is the density of electron states of the surface at the Fermi level, i.e., the tunneling current is proportional to the density of states at the position of the STM point tip. At the same time, replacing the STM point tip with more realistic approximations does not change the conclusion obtained that the STM tip measures the density of states [64].

Oscillations of the density of states can be explained within the framework of a simple model. Consider an adatom as a point defect in a two-dimensional electron gas. If we consider a point defect as a scattering potential with cylindrical symmetry, then the wave function of electrons near the impurity can be written in cylindrical coordinates as $\psi = R_{El}(d) \exp(il\varphi)$ [52], where $R_{El}(d)$ is the radial part of the wave function of electrons with energy E and angular momentum l, φ is the azimuthal angle, and d is the distance to the defect. Then, the change in the density of states near the point defect can be written as [52, 65]

$$\Delta\rho(d) \propto \sum_{l} \left(\left|R_{El}(d)\right|^2 - \left|J_l(k_0 d)\right|^2\right), \quad (4)$$

where $J_l(k_0 d)$ is the Bessel function of the lth order, which is the radial function of electrons in the absence of scattering.

In the case of low-energy scattering, the change in the density of states is equal to

$$\Delta\rho(d) \propto \frac{1}{k_0 d}\left[\cos^2\left(k_0 d - \frac{\pi}{4} + \delta_0\right) - \cos^2\left(k_0 d - \frac{\pi}{4}\right)\right], \quad (5)$$

where δ_0 is the phase shift of the wave function at $l = 0$. It follows from such a model that a redistribution of the density of states at the Fermi level should occur around an adatom or any other defect on the metal surface, which is recorded by a tunneling microscope (see Fig. 1). Experimental studies [59, 66] have shown that the period of oscillations of the electron density around an impurity on the copper surface is equal to $\lambda_F/2 = 12.5$ Å, where $\lambda_F = 2\pi/k_F$, k_F is the wave vector of the surface electrons at the Fermi level. Taking this fact into account, we can rewrite Eqn (5) as

$$\Delta\rho(d) \propto \frac{\sin\delta_0}{k_F d}\cos\left(2k_F d + \delta_0\right). \quad (6)$$

It should be noted that Eqn (6) was obtained as a limiting case at $d \to \infty$ and $l = 0$. Comparing the theory with experiment shows that Eqn (5) describes well the change in the density of states at the Fermi level around the impurity starting from a distance of about 5 Å. The experimental value of the oscillation period $\lambda_F/2$ (12.5 Å) [59, 66] is also in good agreement with the values calculated within the framework of the density functional theory (13.4 Å) [56, 60].

2.2 Indirect long-range interaction between adatoms

STM image analysis can provide valuable information not only on the distribution of surface electron density around an impurity, but also on the interaction energy of adatoms on the surface located at different distances from each other. To determine the interaction energy of adatoms as a function of the distance between them experimentally, an analysis of many STM images of a surface with adatoms deposited on it is carried out and histograms of the distances between adatoms $g(d)$ are constructed, shown in Fig. 2.

At thermodynamic equilibrium, the interaction energy $E(d)$ of two adatoms is experimentally determined as [55]

$$E(d) = -kT\ln\left[\frac{g(d)}{g_{ran}(d)}\right], \quad (7)$$

where $g_{ran}(d)$ corresponds to the random position of adatoms on the surface, and T is the temperature. The interaction energy for Cu/Cu(111) and Co/Ag(111), which was determined by processing several thousand STM images, is shown in Fig. 2. The similarity of the histograms of distances between adatoms $g(d)$ and the curves $E(d)$ for two different systems (Cu/Cu(111) and Co/Ag(111)) indicates that the scattering of surface electrons is practically independent of the elemental composition of the system. However, there are two differences. The first is the different period of oscillations: for Cu(111), $\lambda_F/2 = 12.5$ Å, and for Ag(111), $\lambda_F/2 = 38$ Å. The second is that, for the Ag(111) surface, the absolute values of energy are lower, since the surface has a lower electron density, and the bottom of the Shockley zone of states for Ag(111) is closer to the Fermi level than for the Cu(111) surface [55].

Let us consider the interaction of two adatoms placed on the surface of a metal at distance d from each other, the position of which is determined by radius vectors $\mathbf{r}_A$ and $\mathbf{r}_B$. The potential energy at a point with radius vector $\mathbf{r}$ can be

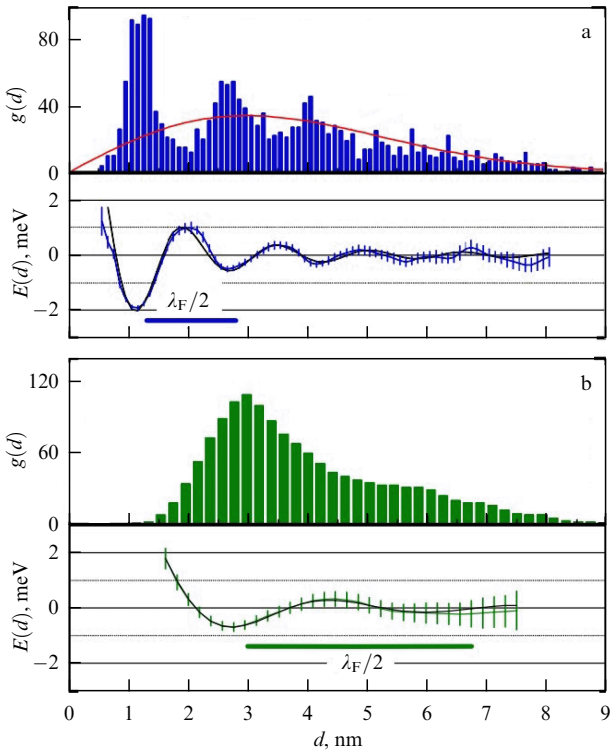

Figure 2. Histogram of distances between adatoms $g(d)$ and energy $E(d)$ of interaction between adatoms for (a) Cu/Cu(111) and (b) Co/Ag(111) [55], calculated using Eqn (7). Line on upper plot corresponds to random distribution of distances between adatoms.

represented as a sum of the potential energies of individual adatoms:

$$U(\mathbf{r}) = U_A\left(|\mathbf{r} - \mathbf{r}_A|\right) + U_B\left(|\mathbf{r} - \mathbf{r}_B|\right). \quad (8)$$

In the second order of perturbation theory, the correction to the energy of the ground state is

$$\Delta E = \sum_i \frac{\left|\langle i\,|U|0\rangle\right|^2}{E_0 - E_i}, \quad (9)$$

where $|0\rangle$ and $|i\rangle$ are the vectors of the ground and the ith excited state of the electron gas. From Eqns (8) and (9), the expression for the interaction energy of two adatoms follows:

$$\Delta E_{int} = \sum_i \frac{\langle 0|U_B|i\rangle\langle i\,|U_A|0\rangle}{E_0 - E_i} + \text{c.c.} \quad (10)$$

If the Fermi surface of the surface states is cylindrical, then the difference between the energies of the ground and excited states of the electron gas is [65]

$$E_0 - E_i = \frac{1}{2m^*}(p^2 - p'^2) = -\frac{1}{2m^*}(q^2 - 2\mathbf{qp}), \quad (11)$$

where m^* is the effective mass of surface electrons, and $\mathbf{p}$ and $\mathbf{p}'$ are two-dimensional wave vectors parallel to the surface, $\mathbf{q} = \mathbf{p} - \mathbf{p}'$. Substituting the expression for the energy difference (11) into Eqn (10), we obtain

$$\Delta E_{int} \propto \sum_{\mathbf{p},\mathbf{q}} \frac{\exp\left(i\mathbf{qd}\right)}{-(1/2)(q^2 - 2\mathbf{qp})}. \quad (12)$$

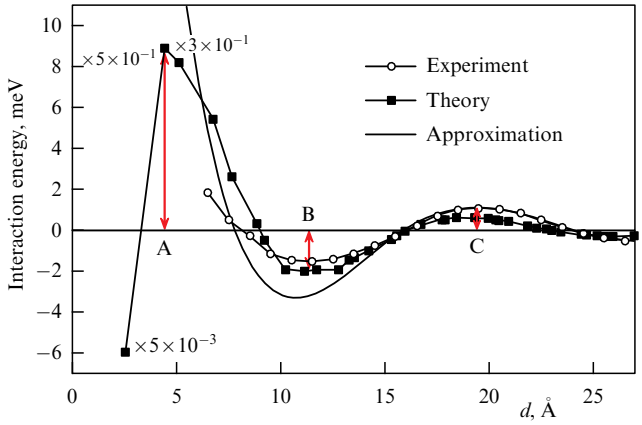

Figure 3. Interaction energy of two cobalt adatoms on Cu(111) surface. Black line is theoretical curve, circles indicate interaction energy calculated within the framework of density functional theory, and black squares indicate experimental values [56]. Letters A, B, C indicate extrema of interaction energy. Approximation is based on Ref. [67].

Table. Parameters of interaction energy on Cu(111) surface [68]. All values are given in meV.

	Ti	V	Cr	Mn	Fe	Co	Ni
A	72.40	44.10	26.40	30.50	32.20	28.30	26.50
B	−0.49	−1.02	−0.69	−1.48	−1.80	−2.02	−2.06
C	0.13	0.20	0.24	0.49	0.57	0.61	0.54

Moving from the sum to the integral and performing the integration, we find [65]

$$\Delta E_{\rm int} \propto \frac{\cos\left(2k_{\rm F}d\right)}{d^2}\,. \qquad (13)$$

A more accurate consideration is given by the expression [67]

$$\Delta E_{\rm int} = -\epsilon_{\rm F}\left(\frac{2\sin\left(\delta_{0,\rm F}\right)}{\pi}\right)^2 \frac{\sin\left(2k_{\rm F}d + 2\delta_{0,\rm F}\right)}{\left(k_{\rm F}d\right)^2}\,, \qquad (14)$$

where $\epsilon_{\rm F}$ is the Fermi energy, measured from the bottom of the band of Shockley states, and $\delta_{0,\rm F}$ is the phase shift during the scattering of surface electrons with $l = 0$ by the adatom.

Oscillations of the density of states at the Fermi level give rise to oscillations in the energy of interaction between adatoms on a metal surface. In Fig. 3, the circles show the experimental values of the energy of interaction between two Co adatoms on the Cu(111) surface, depending on the distance between them. The black squares in Fig. 3 show the interaction energy values calculated within the framework of the density functional theory [52]. It is evident that theoretical and experimental curves of the interaction energy of Co adatoms on the Cu(111) surface are in good agreement, especially at large distances. The characteristic parameters of the interaction energy, indicated in Fig. 3, for 3d metal adatoms are given in the Table. Evidently, they are of the same order of magnitude for all 3d metal adatoms on the Cu(111) surface [68]. Thus, the type of adatom has little effect on the nature of the long-range interaction between them.

2.3 Formation and stability of superlattices

Long-range interaction of adatoms on metal (111) surfaces can lead to the formation of superlattices [66, 69–76]. Examples of such lattices are shown in Fig. 4, where the

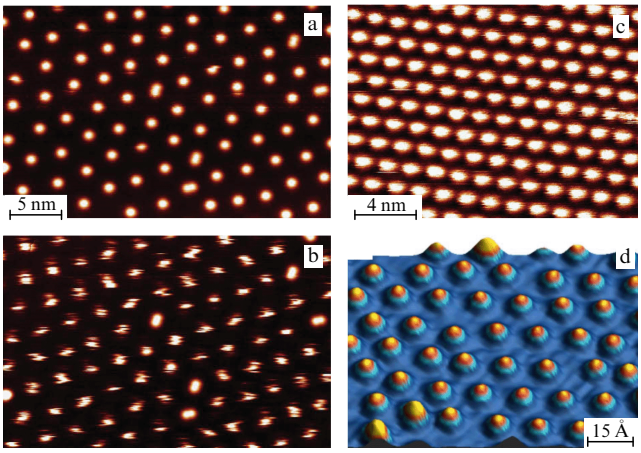

Figure 4. Images of superlattices: (a) Ce/Ag(111) ($T = 3.9$ K), (b) Ce/Ag(111) ($T = 4.8$ K) [69], (c) Na/Cu(111) ($T = 3.9$ K) [70], (d) Fe/Cu(111) ($T = 12$ K) [77].

bright spots are cerium and sodium adatoms. In Ref. [69], it was shown that a 1% coverage of the Ag(111) surface with cerium atoms leads to the formation of an ordered hexagonal arrangement of adatoms (Fig. 4a). A similar picture is observed for sodium atoms on the Cu(111) surface with a coverage of 4% (Fig. 4b). In this case, hexagonal superlattices are formed with distances between two adjacent adatoms of 3.2 nm for Ce/Ag(111) and 1.5 nm for Na/Cu(111).

Superlattices of adatoms are formed only at low temperatures. For example, the STM image shown in Fig. 4a was obtained at a temperature of 3.9 K. At temperatures above 4.8 K, it is impossible to obtain a clear image of the superlattices, because the cerium atoms begin to diffuse over the surface. At temperatures above 5.2 K, there is no long-range order in the Ce/Ag(111) system [78]. Ce atoms move like 'liquid' particles, but the distance between them remains large (approximately 3 nm). The superlattice is destroyed when the adatoms have enough energy to leave the local minimum B in Fig. 3. At a temperature of 8.0 K, the adatom has enough energy to overcome the barrier A (see Fig. 3), dimers are formed, and compact structures grow further. Therefore, there is a temperature range between 3.9 K and 5.2 K in which a superlattice of cerium atoms on the surface of Ag(111) can form because of self-arrangement. The upper limit of the temperature range is determined only by the parameters of the long-range interaction [78]. The lower limit of the temperature range is determined only by the value of the diffusion barrier for the jump of an adatom on the surface [78]; for Ce/Ag(111), it is equal to 10.9 meV [55].

Thus, for the formation of superlattices in the self-arrangement process, it is necessary that the diffusion barrier for the adatom to jump along the surface be small, and the values of the parameters A, B, C (see Fig. 3) of the interaction energy be large.

2.4 Conductivity spectrum of superlattices

The formation of a superlattice on a metal surface leads to a change in the electronic properties of the surface. The conductivity spectrum of the surface Ag(111) (Fig. 5a) was measured at the point marked with an asterisk in the inset of Fig. 5a [74]. The measurements were carried out at a lower temperature (3.3–3.9 K). The temperature of the conductivity spectrum measurement was chosen below the temperature of

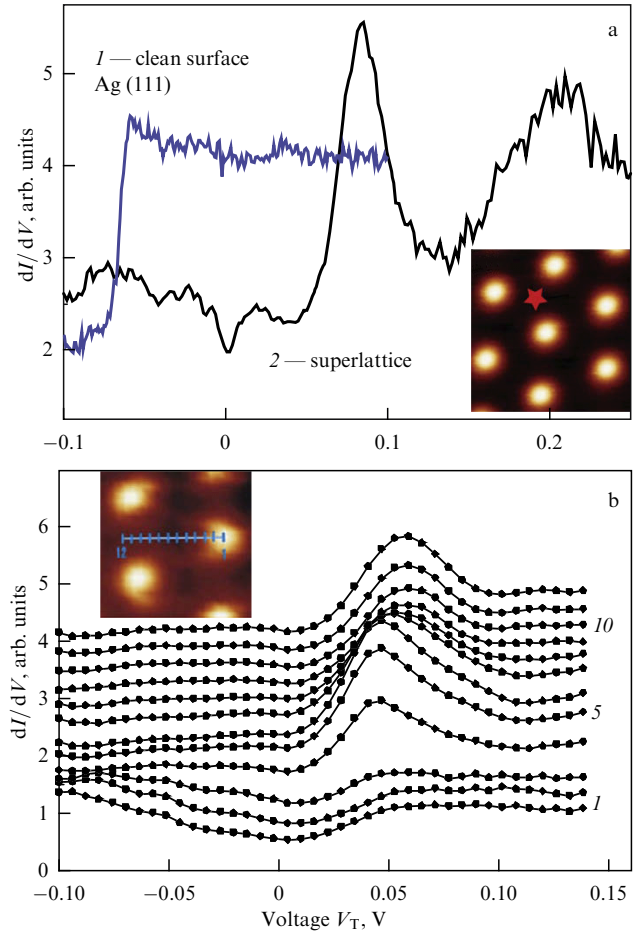

Figure 5. (a) Conductivity spectrum of a pure Ag(111) surface (*1*) and a surface with a superlattice (2). Inset: STM image (7.5×7.5 nm^2) of a hexagonal unit cell of cerium adatom superlattice. Red asterisk in inset marks point where conductivity spectrum was measured. (b) Conductivity spectra measured in hexagonal superlattice with a distance of 3.5 nm between adatoms. In inset, dashes mark positions where conductivity spectrum was measured. Curves *1–3* correspond to position near an adatom, *4–6* to position equidistant from three adatoms, and *10–12* to position between two adatoms [70, 74].

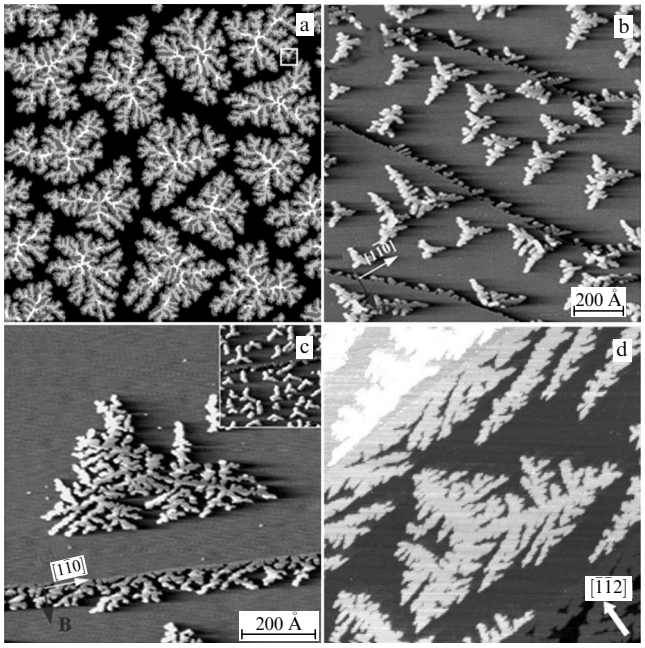

Figure 6. Images of flat dendrites formed on surface of metals: (a) result of Monte Carlo simulation of Co/Cu(111) dendrites at a temperature of 135 K [42], (b–d) STM images of Ag/Ag(111) dendrites at a temperature of 110 K, Ag/Pt(111) dendrites at a temperature of 130 K (80 K in the inset) [41], and Au/Ir(111) dendrites at room temperature [82], respectively.

superlattice formation to prevent adatoms from moving during the measurement.

The conductivity spectrum of the surface in the presence of a superlattice (curve *2* in Fig. 5a) differs radically from that of the pure Ag(111) surface (curve *1* in Fig. 5a). Instead of a step in the conductivity spectrum at 63 meV, the conductivity spectrum of the surface with a superlattice has two pronounced peaks at 85 and 210 meV. The conductivity spectra obtained at different points on the surface are shown in Fig. 5b. Curves *1–3* were measured near the adatom (see the inset in Fig. 5b). They have a dip, resembling an energy gap, between −75 meV and 35 meV. As the STM tip moves away from the adatom to the geometric center of the triangle formed by three cerium adatoms, a peak appears (curves *4–6* in Fig. 5b). The maximum value of the peak is observed at an energy of 45 meV. The position of this peak in the conductivity spectra depends significantly on the interatomic distance. The average interatomic distance in the superlattice depends on the degree of coverage. For cerium superlattices, it varies from 2.3 nm to 3.5 nm. As the interatomic distance decreases, the position of the peak shifts toward higher energies.

Metal-organic frameworks (MOFs) can be classified as superlattices. These structures consist of metal atoms and organic linker molecules that bind them and are distinguished by a very large variability of their structural elements. MOFs can be defined as quasi-crystalline structures, since they have a long-range order, although translational symmetry is often absent. The field of science studying MOFs was formed at the intersection of physics and chemistry and is currently very extensive. We will not consider MOFs in this review but will restrict ourselves to mentioning existing review papers [79–81].

3. Flat dendrites

The simplest example of flat dendrites that are often found in nature are the ice patterns on windowpanes familiar to everyone since childhood. In metallic homoepitaxial and heteroepitaxial systems, the growth of clusters in the form of flat dendrites is also often observed. For example, in the Co/Cu(111) system [42], flat dendrites are formed when the temperature is lowered to 135 K (Fig. 6a). At temperatures of $\sim$ 100 K, the growth of flat dendrites from Ag atoms is observed on the surfaces of Ag(111) (Fig. 6b) and Pt(111) (Fig. 6c) [41]. The growth of flat dendrites from Au atoms on the surface of Ir(111) (Fig. 6d) can occur even at room temperature [82]. It is important to note that the growth of flat dendrites is a result of self-arrangement of atoms and therefore can be controlled by changing external conditions such as substrate temperature and atomic deposition rate.

The shape of flat dendrites is related to the symmetry of the substrate surface. If flat dendrites grow on the (110) surface of a face-centered cubic (FCC) crystal, they have a symmetry axis of the second order directed perpendicular to the surface; if flat dendrites grow on the (001) surface of an FCC crystal, they have a symmetry axis of the fourth order

[83]. On the (111) surfaces of FCC crystals or the (0001) surfaces of hexagonal close-packed (HCP) crystals, the growth of flat dendrites occurs in a more complex way. On such surfaces, two types of steps (A and B) are possible. If the energies of atoms on steps A and B differ, this leads to the appearance of anisotropy of diffusion barriers for bypassing the corners of the growing cluster. As a result, the formation of flat dendrites with a third-order symmetry axis is observed. The growth of such dendrites was experimentally detected in the epitaxial systems Au/Pt(111) [84], Co/Cu(111) [42], Co/Pd(111) [85], Co/Re(0001) [86], Pt/Ru(0001) [87], Pd/Cu(111) [88]. If the anisotropy of diffusion barriers for bypassing the corners of the cluster can be disregarded, in comparison with the energy of thermal motion, then flat dendrites will have a sixth-order symmetry axis. The formation of flat dendrites of this type was detected at a temperature close to room temperature in such epitaxial systems as Au/Ru(0001) [89], Ag/Pt(111) [90], and Fe/Ag(111) [91]. If the energy of thermal motion is comparable to the anisotropy of diffusion barriers for bypassing the cluster corners, then flat dendrites acquire some intermediate shape that does not have any pronounced symmetry. Such asymmetric flat dendrites are formed, for example, in the epitaxial system Ag/Ni(111) at a temperature below 800 K [92] and in the Ag/Re(0001) system at room temperature [93].

The shape of substantially branched dendrites can be characterized by the fractal dimension D_f [94]. By definition [39, 40], the fractal dimension D_f is the limit

$$D_f = \lim_{\epsilon \to 0} \frac{\ln N(\epsilon)}{\ln (1/\epsilon)}\,, \tag{15}$$

where $N(\epsilon)$ is the minimum number of n-dimensional cubes with side ϵ required to cover the fractal, with n being the dimension of the space in which the fractal is formed (in our case, $n = 2$, since we are considering flat dendrites). For practical calculation of the fractal dimension of dendrites, one of three approximate methods is commonly used [94]. In the first [94], based on definition (15), the fractal dimension is found from the slope of the linear dependence $\ln N(\epsilon) = \text{const} - D_f \ln \epsilon$. Another widely used method for calculating the fractal dimension of dendrites is to plot the dependence of the dendrite mass on its radius [82, 94]. Indeed, if a dendrite is covered with a system of concentric n-dimensional spheres with the center coinciding with the dendrite growth center, then the number of atoms $N(R)$ inside a sphere of radius R will be proportional to the value of R^{D_f}. Therefore, the fractal dimension of a dendrite can be found from the slope of the linear dependence $\ln N(R) = \text{const} + D_f \ln R$. The third method for calculating the fractal dimension of a cluster is based on its relation to the correlation function [94, 95] of dendrite atoms

$$C(\mathbf{r}) = N^{-1} \sum_{\mathbf{r}'} \rho(\mathbf{r}')\, \rho(\mathbf{r}' + \mathbf{r})\,, \tag{16}$$

where N is the number of atoms in the cluster, and the density $\rho(\mathbf{r}) = 1$ if the crystal lattice node is occupied by an atom, and $\rho(\mathbf{r}) = 0$ otherwise. For flat dendrites, the relation $C(r) \sim r^{D_f - 2}$ is satisfied [95]. Therefore, the fractal dimension can be found from the slope of the linear dependence $\ln C(r) = \text{const} + (D_f - 2) \ln r$. The details of applying these methods to finite-size dendrites are discussed in monograph [94].

Theoretical methods for studying the formation of dendrites can be divided into three groups: (1) methods based on the approximation of a continuous medium [38, 96], (2) various variations of the diffusion-limited aggregation (DLA) model [95, 97], and (3) the kinetic Monte Carlo method. Methods based on the continuous medium approximation are commonly used to describe the growth of dendrites in a two-component supercooled system. Their description is beyond the scope of our review. Readers can familiarize themselves with the current state of this issue in review [38].

First, let us dwell in more detail on the description of the DLA mechanism, according to which a certain type of dendrite can be obtained in the process of disordered irreversible growth. Let us imagine a dendrite growing in the following way [37]: over time, an atom joins it and immediately 'sticks' to it. It is assumed that all atoms move randomly. If an atom joins an initially compact dendrite nucleus, a protrusion is formed, and the cluster growth in this place will accelerate. As a result, the slightly distorted shape of the nucleus is deformed even more, i.e., unstable growth occurs, resulting in the formation of a disordered, highly sparse structure — a dendrite (fractal cluster). An example of such a structure, consisting of 5000 atoms, is shown in Fig. 7a. It is worth noting the similarity of the obtained cluster to the Lichtenberg figure (Fig. 7b), formed in a dielectric during breakdown [98]. This similarity is not accidental, since the formation of dendrites within the DLA framework is described by the Laplace equation, which is also satisfied by the scalar potential in electrostatics problems.

The main advantage of the described method is that it shows the relation between the process of dendrite growth and its fractal dimension. Based on a simple dimensional analysis [99], one can obtain a formula for the fractal dimension of dendrites in the DLA method:

$$D_f = \frac{D^2 + D_1 - 1}{D + D_1 - 1}\,, \tag{17}$$

where D is the dimension of the space in which the dendrite grows, and D_1 is the dimension of the trajectory of the atoms' movement ($D_1 = 2$ in the case of Brownian motion). According to this formula, the fractal dimension of flat dendrites is $D_f^{(2)} = 5/3$, and the fractal dimension of volumetric dendrites is $D_f^{(3)} = 5/2$. This result is in good agreement with those from computer modeling [100].

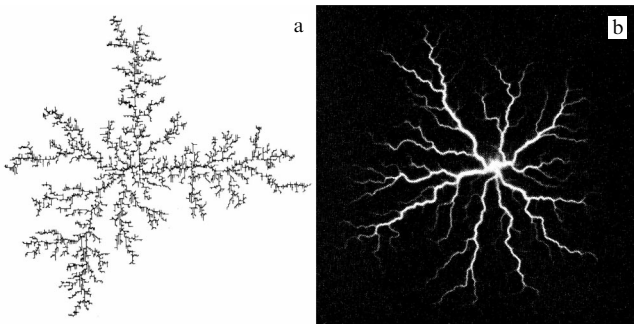

Figure 7. (a) Cluster of 5000 particles obtained within diffusion-limited aggregation model. (b) Lichtenberg figure formed due to dielectric breakdown. (Figures adopted from [98].)

A comparison of Figs 6 and 7 shows that the shape of fractal clusters obtained within the DLA method differs significantly from the shape of flat dendrites formed on the surface of crystals. Flat dendrites not only have a certain symmetry but also look significantly 'thicker' than dendrites obtained by DLA modeling. This means that the fractal dimension of flat dendrites takes the values $5/3 \leqslant D_f^{(2)} \leqslant 2$. To describe the fractal dimension of real flat dendrites, a generalized DLA (GDLA) model is used [82, 101], within which diffusion of atoms along the dendrite boundaries with a certain effective diffusion barrier ΔE_{edge} is introduced. According to this model, the fractal dimension of a flat dendrite is

$$D_f = \frac{4\sqrt{\nu_0\tau}\exp\left(-\Delta E_{edge}/2k_BT\right)+5}{2\sqrt{\nu_0\tau}\exp\left(-\Delta E_{edge}/2k_BT\right)+3}, \qquad (18)$$

where ν_0 is the frequency prefactor for an atom's jump along the surface, τ is the average time of atom diffusion along the cluster edge, k_B is the Boltzmann constant, and T is the surface temperature. The value of $\sqrt{\nu_0\tau}$, as a rule, is much greater than unity. Therefore, at high temperatures $T \geqslant E_{edge}/2k_B$, the fractal dimension is close to 2, which corresponds to the formation of compact clusters, and at low temperatures, $T \ll E_{edge}/2k_B$, the fractal dimension tends to 5/3, which corresponds to a maximally branched dendrite.

Let us now proceed to a description of dendrite formation modeling by the kinetic Monte Carlo (KMC) method [102, 103] or its 'smarter' version — the self-learning KMC method [104–106]. The KMC method allows demonstrating the influence of the effective diffusion barrier ΔE_{edge} and the anisotropy of diffusion barriers near the cluster corners on the shape of a flat dendrite [82]. It is clearly seen from Fig. 8 that, the smaller the effective barrier ΔE_{edge}, the closer the dendrite shape approaches a compact cluster, and considering the anisotropy of barriers for bypassing corners leads to a change in the symmetry of both compact clusters and dendrites. Another successful example of KMC modeling is the study of the growth of two-layer Co clusters on the Cu(111) surface (Fig. 6a). The results of the simulation and the experimentally obtained STM image [42] are qualitatively indistinguishable from each other.

It follows from the above examples that the results of Monte Carlo simulation of single-component dendrites are in qualitative agreement with Eqn (18). The situation, however, is significantly more complicated in the case of two-component dendrites. As an example, let us consider the formation of clusters consisting of Pt and Cu atoms on the Cu(111) surface. Usually, in the experiment [43, 107, 108], Pt atoms are deposited on the surface by molecular beam epitaxy. In this case, Pt atoms can be embedded in the copper surface, pushing out Cu atoms. As a result, the embedded platinum atoms become growth centers for the clusters, and the clusters themselves are formed from a mixture of Pt and Cu atoms. We emphasize that the experimental data [43, 107, 108] do not allow answering the question of which atoms (Cu or Pt) the clusters on the Cu(111) surface consist of.

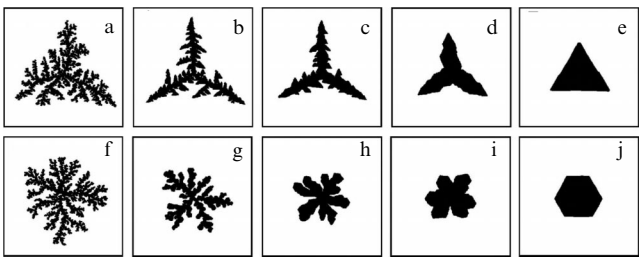

Figure 8. Results of modeling growth of flat dendrites on (111) surface of FCC crystal in the absence (a–e) and presence (f–j) of anisotropy of diffusion barriers for bypassing corners [82]. Clusters were obtained at temperature of 300 K and at different values of effective diffusion barrier ΔE_{edge} for motion of an atom along cluster edge: (a) 0.80 eV, (b) 0.60 eV, (c) 0.53 eV, (d) 0.48 eV, (e) 0.35 eV, (f) 0.85 eV, (g) 0.58 eV, (h) 0.50 eV, (i) 0.40 eV, (j) 0.25 eV. Each cluster consists of 20,000 atoms.

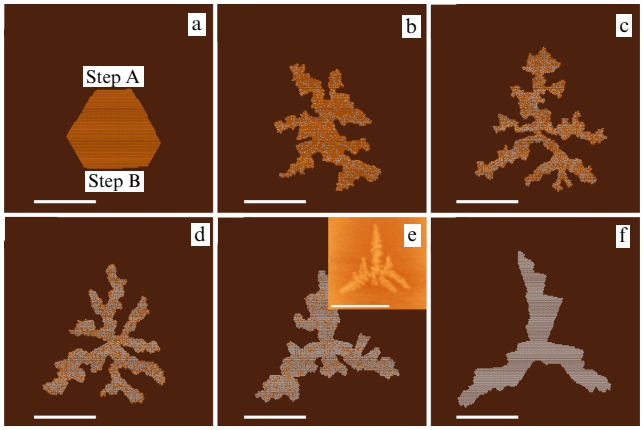

Figure 9. Images of computing domain (top view) obtained as a result of simulation [109] of deposition of 4000 atoms on a Cu(111) surface at a substrate temperature of 300 K. Relative concentration of Pt atoms is 0 (a), 0.2 (b), 0.4 (c), 0.6 (d), 0.8 (e), and 1 (f). Scale bar is 10 nm. Orange and gray balls represent Cu and Pt atoms, respectively. Inset in e shows image of experimentally observed cluster [107].

Let us consider the results of modeling the growth of flat clusters at different ratios of platinum n_{Pt} and copper n_{Cu} concentrations in the cluster [109]. Let us introduce a dimensionless parameter, the relative concentration of platinum atoms $n = n_{Pt}/(n_{Cu} + n_{Pt})$, varying from 0 to 1. With an increase in the relative concentration of platinum, two effects are observed (Fig. 9): a change in the symmetry of the cluster and a nonmonotonic change in its fractal dimension. The first effect is associated with a monotonic increase in the anisotropy of diffusion barriers for bypassing the corners of the cluster with an increase in the platinum concentration. The second effect is due to the nonmonotonic change in the effective barrier ΔE_{edge}. The fractal dimension D_f found from the results of the KMC simulation can be approximated by Eqn (18), and the effective barrier ΔE_{edge} turns out to be a function of the relative concentration of platinum atoms n. In the simplest case, the function $\Delta E_{edge}(n)$ can be considered a cubic polynomial with a maximum at $n = 0.45$ [109]. Comparing the results of the simulation [109] and the experimentally obtained STM image [107] (see the inset in Fig. 9e), it can be concluded that, when Pt atoms are deposited on the Cu(111) surface at room temperature, the flat dendrites formed in the experiment consist of 80% Pt atoms and 20% Cu atoms.

It should be noted that the formation of flat dendrites occurs not only on flat areas of the surface, but also near steps (Fig. 6b, c). We will discuss the formation of such dendrites in Section 4.

Interest in dendritic clusters is associated not only with their beauty, but also with their unusual physical and

chemical properties, primarily with high catalytic activity [110–112]. The increase in the catalytic activity of dendrites compared to compact clusters is associated with an increase in both their surface area and surface energy (per unit area) due to the appearance of a large number of faces with high Miller indices.

4. Finger-like protrusions

Finger-like protrusions are a very exotic type of nanostructure, so let us first explain what we mean by a 'finger-like protrusion.' As is known [113], there are always steps on the surface of a crystal. And, in the absence of defects, such steps should have a minimum length, i.e., they should be even. However, if the number of impurity atoms near the steps is increased, then under certain conditions it is possible to achieve a significant curvature of the steps and the formation of elongated formations, resembling fingers in shape [43, 44]. The simplest way to saturate a surface with point defects is to sputter atoms of another metal onto the surface of a metal. In this case, for the resulting bimetallic system, it is required, first, that the impurity atoms remain on the surface, and second, that they actively mix with the substrate atoms near the steps. Thus, the formation of finger-like protrusions is possible in bimetallic systems that can form a surface alloy.

Extensive literature is devoted to binary surface alloys (see, e.g., monograph [114]). As an example, let us consider the surface alloy Pt/Cu(111). Experimental study [115] of the early stage of surface alloy Pt/Cu(111) formation showed that the platinum and copper atoms are most intensively mixed near the atomic steps on the surface of Cu(111). At the same time, as theoretical calculations have shown, the main factors affecting the formation of the Pt/Cu(111) alloy are [116]: (1) the formation of Pt–Cu chemical bonds, (2) the magnitude of the energy of attraction between the Cu and Pt atoms, (3) the difference between the lattice constant values for copper and platinum crystals.

Let us consider in more detail the formation of the Pt/Cu(111) surface alloy with a low degree of coverage of the Cu(111) surface with platinum $\eta \leqslant 10\%$ [43, 44]. As can be seen from Fig. 10, the structure of the forming surface alloy depends significantly on both the substrate temperature and the number of Pt atoms deposited on the surface. When platinum is deposited at a temperature of 550 K, a disordered Pt/Cu(111) surface alloy is formed with a uniform distribution of Pt atoms on the surface (Fig. 10a). When the same amount of platinum is deposited at a temperature of 450 K, the distribution of Pt atoms embedded in the first layer is uneven: their concentration increases near the step (Fig. 10b). At a temperature of 315 K, the surface alloy is formed only near the atomic steps on the surface of Cu(111), and with a small number of Pt atoms ($\eta = 3\%$), the edge of the step becomes curved, and small protrusions consisting mainly of copper atoms are formed on the step (Fig. 10c). With an increase in the degree of surface coverage with Pt atoms to 10%, the length of the finger-like protrusions increases significantly (Fig. 10d). Upon closer examination of these protrusions (Fig. 10e), small areas of ordered surface alloy with a $p(2 \times 2)$ structure (Fig. 10f) or $(\sqrt{3} \times \sqrt{3})R30$ (Fig. 10g) are found in them. In addition, as can be seen from Fig. 10d, in addition to the finger-like protrusions, clusters are formed on the Cu(111) surface, the structure of which exactly coincides with that of the finger-like protrusions. Note that such clusters are completely different from the flat dendrites growing in the Pt/Cu(111) epitaxial system at room temperature [107, 109]. A significant difference between the finger-like protrusions and the dendrites considered in Section 3 is that, first, they are not self-similar, and second, they mainly consist of substrate atoms.

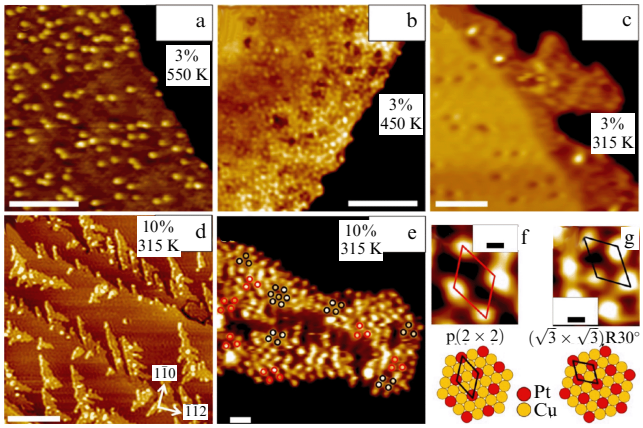

Figure 10. STM images [43] of Pt/Cu(111) surface alloy formed at different temperatures T and degrees of surface coverage η with platinum: (a) $T = 550$ K, $\eta = 3\%$, (b) $T = 450$ K, $\eta = 3\%$, (c) $T = 315$ K, $\eta = 3\%$, (d, e) $T = 315$ K, $\eta = 10\%$. (f, g) Details of ordered surface alloy. Length of scale bar is 5 nm (a–c), 50 nm (d), 1 nm (e), 0.2 nm (f, g).

A qualitative explanation of the experimental results [43] can be given using a simple model, in which there are only three events: (1) diffusion of the Pt atom over the Cu(111) surface, (2) embedding of the Pt atom into the substrate near the step, and (3) embedding of the Pt atom into the substrate on a flat terrace. At a temperature of 315 K, processes 1 and 2 predominate, and at 550 K, processes 1 and 3 predominate. For a deeper understanding of the growth process of finger-like protrusions, Monte Carlo simulations were performed [117, 118]. We will briefly describe the main ideas and results of this work.

The maximum degree of copper surface coverage with Pt atoms was 5%, which corresponds to the experimental conditions [43]. The temperature of the copper substrate varied from 285 K to 345 K. Figures 11b–f show the successive stages of the Pt/Cu(111) surface alloy formation at a temperature of 315 K. As can be seen from these figures, the Pt/Cu(111) surface alloy grows only near the edges of the steps. With an increase in platinum concentration, a growth of finger-like protrusions saturated with Pt atoms is observed. Moreover, the finger-like protrusions on step B are longer than the ones on step A. Four to five finger-like protrusions are usually formed on each step, which corresponds to their average width from 5.1 nm to 6.4 nm.

Let us discuss the formation of ordered sections of the Pt/Cu(111) surface alloy with the $p(2 \times 2)$ or $(\sqrt{3} \times \sqrt{3})R30$ structure, which were observed in experiment [43]. The binding energy of two Pt atoms embedded in the Cu(111) surface at a distance of the second and third nearest neighbors is 0.112 eV and 0.055 eV, respectively. Positive values of the binding energy mean that the arrangement of Pt atoms at distances of the second and third nearest neighbors from each other is unfavorable from the point of view of energy. According to the results of modeling [117], Pt atoms are distributed randomly near the step boundaries. In this case, some of them indeed find themselves at distances of the

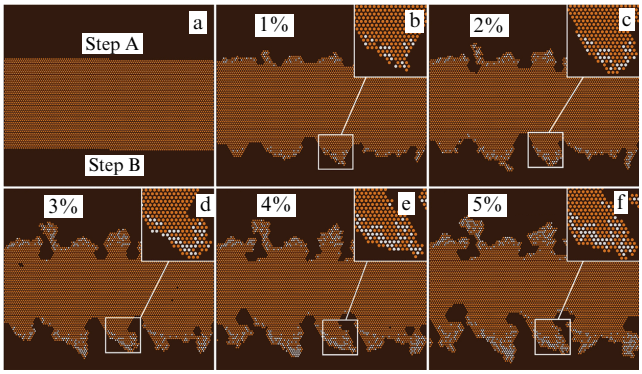

Figure 11. Successive images of computing domain obtained during simulation of deposition of Pt atoms on Cu(111) surface [117]: (a) initial configuration, (b–f) successive configurations corresponding to degree of surface coverage by platinum atoms $\eta = 1-5\%$. Temperature of copper substrate is 315 K. Cu atoms are depicted as orange balls, Pt atoms, as gray balls. Insets show details of one of the finger-like protrusions.

second or third nearest neighbors from each other, which corresponds to the experiment [43].

In experimental study [43], the growth of not only finger-like protrusions but also clusters of Cu and Pt atoms located near the steps was observed. When analyzing the results of the simulation in [117], it becomes obvious that the formation of such clusters is associated with the separation of long finger-like protrusions from the step, which occurs due to their thinning at the base. The formation of such clusters occurs only at a sufficiently low platinum deposition rate, at which the finger-like protrusions on the steps are sufficiently long and thin.

Finally, it was shown in [117] that the length of the finger-like protrusions increases with increasing temperature. In this case, the probability of the formation of Pt–Cu clusters also increases. At all temperatures in the range of 315 ± 30 K, the finger-like protrusions on step B are longer than those on step A. Their average length increases monotonically with increasing platinum concentration. At temperatures below 285 K, the Cu and Pt atoms at the edges of the steps are barely mixed and the formation of finger-like protrusions does not occur.

A significantly greater diversity of nanostructures formed near the steps can be achieved by simultaneous deposition of Pt and Cu atoms on the Cu(111) surface. In Ref. [119], such a process was simulated with different ratios of deposited Pt and Cu atoms. Figure 12 shows the results of simulating the deposition of 10,000 atoms on a stepped Cu(111) surface. It is evident that the shape of the resulting clusters depends on three parameters: the temperature T, the relative concentration of platinum $n = n_{Pt}/(n_{Cu} + n_{Pt})$, and the type of step on which the clusters grow. For dendrite growth, the temperature of the system must be lowered to ~ 200 K. However, even under these conditions, dendrites do not form during the deposition of pure copper. Dendrites form only if Pt atoms are added to the system. Note the significant difference between the shapes of the dendrites growing on steps of different types. On step A, dendrites grow that are elongated in the direction perpendicular to the step, and their length weakly depends on the Pt concentration at $n > 0.4$. Under the same conditions, highly branched dendrites grow on step B. The length of their boundary is maximum at $n = 0.4$ and decreases at a higher Pt concentration. Note the visual similarity of the dendrites formed on step B and the

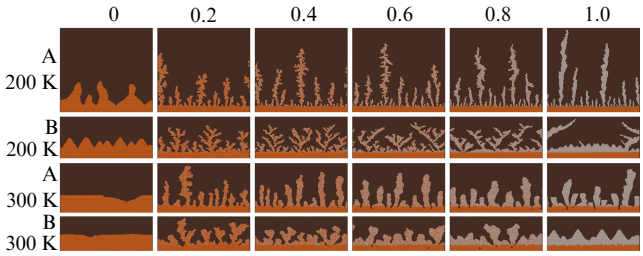

Figure 12. Images of part of computing domain (top view) after deposition of 10,000 atoms [119]. Orange and gray balls show Cu and Pt atoms, respectively. Relative concentration of platinum is shown in figure above, with system temperature and step type (A or B) labeled on left.

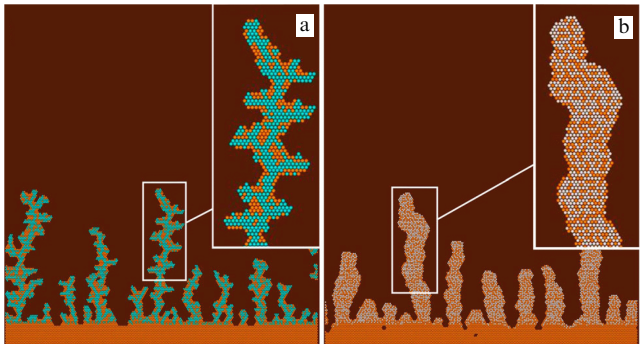

Figure 13. Result of modeling [120] the formation of finger-like protrusions on step A of Cu(111) surface from atoms of (a) Co and Cu, (b) Pt and Cu. Temperature 300 K, relative concentration of impurity atoms (Co or Pt) $n = 0.6$. Orange, blue, and gray balls show atoms of Cu, Co, and Pt, respectively. Insets show details of finger-like protrusions.

experimentally observed dendrites shown in Fig. 6c. At room temperature, no dendrites are formed. Instead, finger-like protrusions grow on the steps, which inherit the shape of the dendrites described above. That is, on step A, the protrusions are longer and thinner than the ones on step B. In the case of deposition of pure platinum, the protrusions on step B acquire a pronounced triangular shape.

Similar results are obtained when simulating the simultaneous deposition of Co and Cu atoms on the Cu(111) surface [120]. However, a significant difference between the Pt/Cu and Co/Cu systems is that the dimerization energy of the embedded platinum atoms is positive (0.15 eV), while the dimerization energy of the cobalt atoms is negative (−0.12 eV), i.e., it is energetically favorable for the Co atoms embedded in copper to form bound structures. This leads to interesting consequences. For example, Fig. 13 shows finger-like protrusions of Co and Cu atoms (Fig. 13a), as well as of Pt and Cu atoms (Fig. 13b), growing on the Cu(111) surface under the same conditions. It is evident that the finger-like protrusions of Co and Cu atoms have a clearly expressed skeleton of Co atoms covered with Cu atoms.

The practical application of finger-like protrusions, as well as dendrites, is currently associated mainly with their use as catalysts. Thus, in Ref. [44], it was shown that the diluted surface alloy Pt–Cu, formed in finger-like protrusions, can be an efficient catalyst for hydrogenation reactions at a significantly reduced concentration of the precious metal. In addition, if the above-described results [120] on the formation of finger-like protrusions with a skeleton of Co atoms are experimentally confirmed, it should be expected that such

nanostructures will have interesting magnetic properties and can find practical application.

5. Nanostructures in first layer of surface

As shown in Section 4, when the temperature of the metal substrate increases (usually by several hundred degrees above room temperature), the atoms deposited on it are embedded in the surface layers of the substrate. When the energy of interatomic chemical interaction is negative, there is a tendency toward ordering and a surface alloy is formed [121]; when the sign is positive, there is a tendency toward stratification and bound nanostructures are formed, embedded in the surface layers of the substrate. Let us consider the case when the embedding of atoms in the substrate occurs much faster than the formation of bound nanostructures. In this case, the formation of nanostructures in the surface layers of the substrate can be divided into two stages: the embedding of atoms in the surface layers and the formation of certain structures due to the diffusion of embedded atoms.

At the first stage, impurity atoms are deposited on a metal substrate and the metal surface is calcined. The calcination temperature depends on the surface properties and the type of deposited atoms. For example, the calcination temperature of the Cu(001) surface, required for embedding Pd, In, and Co atoms, is 425 K [122], 675 K [123], and 800 K [45], respectively. After calcination, the sample is usually cooled to room temperature or slightly higher, at which the impurity atoms remain mobile and diffuse in the first surface layer of the metal.

The diffusion of impurity atoms in the first layer of a metal substrate has been studied experimentally using STM [45, 122–125]. For example, the diffusion of embedded In atoms in the first layer of a Cu(001) surface has several peculiarities [123]. First, In atoms jump quite rarely: at room temperature, the interval between successive jumps of one atom can be several minutes. Second, In atoms typically move several interatomic distances at once instead of making short jumps covering the distance to their nearest neighbors on the surface. Third, correlated diffusion of neighboring In atoms is observed. To explain such an unusual behavior of the embedded impurity atoms in the Cu(001) surface, we can imagine a few possible mechanisms of diffusion of the embedded atoms [123]: (1) the diffusion of the embedded atoms is due to the presence of adsorbed gas molecules on the surface, (2) the diffusion of the embedded atoms occurs through the permutation of the impurity and substrate atoms, and (3) the diffusion of the embedded atoms is a consequence of the intense motion of surface vacancies. Let us discuss these three possible mechanisms of diffusion of the embedded atoms in more detail.

The diffusion of embedded atoms may be associated with the presence of adsorbed gas molecules on the substrate surface. For example, the diffusion of Pt atoms in the Pt(110) surface is a consequence of the presence of adsorbed hydrogen atoms on the surface [126]. However, for a number of reasons [123], this mechanism is unacceptable for the Cu(001) surface. The main reason here is that the adsorbed gas molecules do not stay on the substrate surface for long. In addition, this mechanism cannot explain the unusual behavior of embedded In atoms described above.

The mechanism of diffusion of embedded atoms by means of permutation of impurity and substrate atoms is schematically shown in Fig. 14 [123]: (a) a substrate atom approaches an impurity atom, (b) a substrate atom displaces an impurity atom from the substrate, and (c) an impurity atom is embedded in another place on the substrate, displacing the substrate atom from there. Thus, diffusion of embedded atoms is carried out by means of permutation of their places with single substrate atoms, which freely move over the surface. This diffusion mechanism is decisive, for example, for the Cu/Co system on the Ru(0001) surface [124].

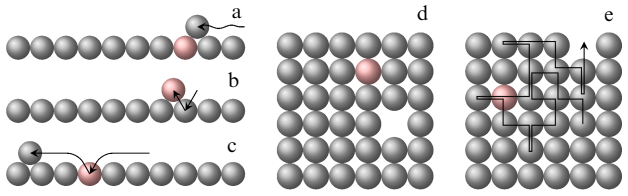

Figure 14. Possible mechanisms of diffusion of impurity atoms in first layer of (001) surface of an FCC crystal [123]: (a–c) diffusion by means of permutation of impurity and substrate atoms, (d, e) diffusion due to movement of surface vacancies.

The mechanism of diffusion of impurity atoms in the first layer of the Cu(001) surface by means of surface vacancies was first proposed to explain the diffusion of Mn atoms [125] and is schematically shown in Fig. 14d, e. In this model, the diffusion of an impurity atom occurs as follows: first, a surface vacancy approaches an embedded impurity atom to the distance of the nearest neighbors, then the impurity atom and the vacancy change places, after which the surface vacancy moves away from the embedded atom and continues to diffuse freely over the substrate surface. This mechanism of diffusion of embedded atoms was also discovered for the diffusion of Pd [122] and Co [45] atoms in the first layer of the Cu(001) surface. As for the diffusion of In atoms in the first layer of the Cu(001) surface [123], it is characterized by two mechanisms of diffusion of embedded atoms, both through substrate atoms and due to the diffusion of surface vacancies.

In order for the 'vacancy' mechanism to be realized, it is necessary that the concentration of surface vacancies be high enough. The relative concentration of vacancies in the volume of the crystal can be calculated as $\exp(-G/k_{\mathrm{B}}T)$ [127], where $G \approx E - TS$ is the Gibbs energy of vacancy formation, S and E is the entropy and energy of vacancy formation, T is the temperature, and, as a rule, $E \gg TS$. Thus, the concentration of vacancies is determined mainly by the energy of their formation. Calculations using the Green's function method [128] showed that, among the 3d-, 4d-, and 5d-metals, the energy of vacancy formation is minimal in Cu, Pd, Ag, Pt, and Au. The concentration of vacancies in these metals is already high enough at room temperature for vacancies to play a significant role in processes associated with the diffusion of impurity atoms. The energies of vacancy formation on the surfaces of Al(111), Cu(111), Ag(111), and Rh(111) calculated by the density functional method turned out to be 30–40% lower than the energies of vacancy formation in the bulk of the same metals [129]. The energies of vacancy formation on the surfaces of metals Ag, Cu, Ni, Pb, Al, and Pd with low Miller indices were calculated by the embedded atom method [130]. It turned out that, first the highest energy of formation of surface vacancies corresponds to the densely packed surface (111), and second, the energy of formation of vacancies on the surfaces (001) and (110) is less than on the surface (111) by 10–25% and 60–65%, respectively. Thus, it is

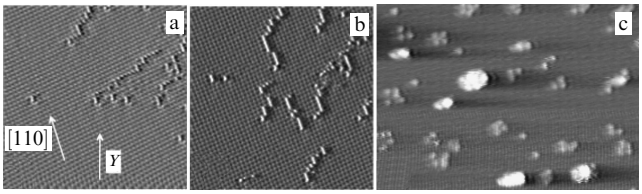

Figure 15. Formation of bound nanostructures from Co atoms in first layer of Cu(001) surface. (a, b) STM images obtained at different potential differences between STM tip and surface [45]: (a) $U = -60$ mV, (b) $U = -170$ mV; Y is direction of movement of STM tip. (c) STM image of compact Co clusters at temperature of 317 K [46].

the faces (110) of the crystal that serve as a source of bulk vacancies [131]. At the same time, the concentration of surface vacancies on the faces (001) is also quite high.

An analysis of the dimer binding energy values [132] allows us to determine whether bound nanostructures or a surface alloy will be formed in the first surface layer. However, the question of the size and shape of the forming structures is more complex. Let us discuss the possible types of bound nanostructures in the first surface layer using the Co/Cu(001) system as an example. In Ref. [45], it was shown that scanning the Cu(001) surface with Co atoms embedded in it can result in the formation of bound chains of Co atoms (Fig. 15a, b). When scanning the surface, the embedded Co atoms move predominantly in the direction of their nearest neighbors ([110]), which forms an acute angle with the direction of the STM tip (Y) (Fig. 15a). In this case, the self-arrangement of the embedded Co atoms is a consequence of the electrical interaction between the STM tip and the Co atoms. Thus, at a potential difference of 23 mV between the surface and the STM tip, the Co atoms remain practically motionless. When the potential difference increases to 60 mV (Fig. 15a) and 170 mV (Fig. 15b), the embedded Co atoms begin to follow the STM tip and form atomic chains. The length of the chain linear sections increases with increasing potential difference between the STM tip and the surface. According to the authors of Ref. [45], this experimental result may be associated with a sharp increase in the concentration of surface vacancies because of the electrical interaction of the copper surface with the STM tip. Two years later, experimental study [46] appeared, in which the diffusion of embedded Co atoms at a temperature of 317 K was studied. In addition to single Co atoms, compact clusters of embedded Co atoms are clearly visible in the STM images obtained (Fig. 15c). The question arises of how to combine the experimental results showing the possibility of forming both compact [46] and noncompact [45] bound Co nanostructures in the first layer of the Cu(001) surface.

This question can be answered by modeling the self-arrangement of nanostructures from Co atoms in the first layer of the Cu(001) surface using the Monte Carlo method [133–135]. To simplify the modeling, two additional assumptions can be made: (1) immediately after deposition, the distribution of Co atoms in the Cu(001) surface is uniform, (2) the influence of Cu atoms displaced from the copper surface can be neglected. Thus, the problem of forming embedded Co nanostructures is reduced to a two-dimensional (single-layer) problem with a constant number of atoms.

According to the results of modeling [134], the evolution of the Co atom system in the first layer of the Cu(001) surface can be divided into three stages: (1) diffusion of adatoms, (2) formation of atomic chains, and (3) formation of compact clusters. A typical surface morphology obtained at a substrate temperature of $T = 400$ K and a concentration of embedded atoms of $n_{Co} = 10\%$ at each of the three stages is shown in Fig. 16a–c. At the first two stages of evolution, mainly dimers and small bound nanostructures of three to four atoms are formed: trimers and quadromers. All possible bound nano-

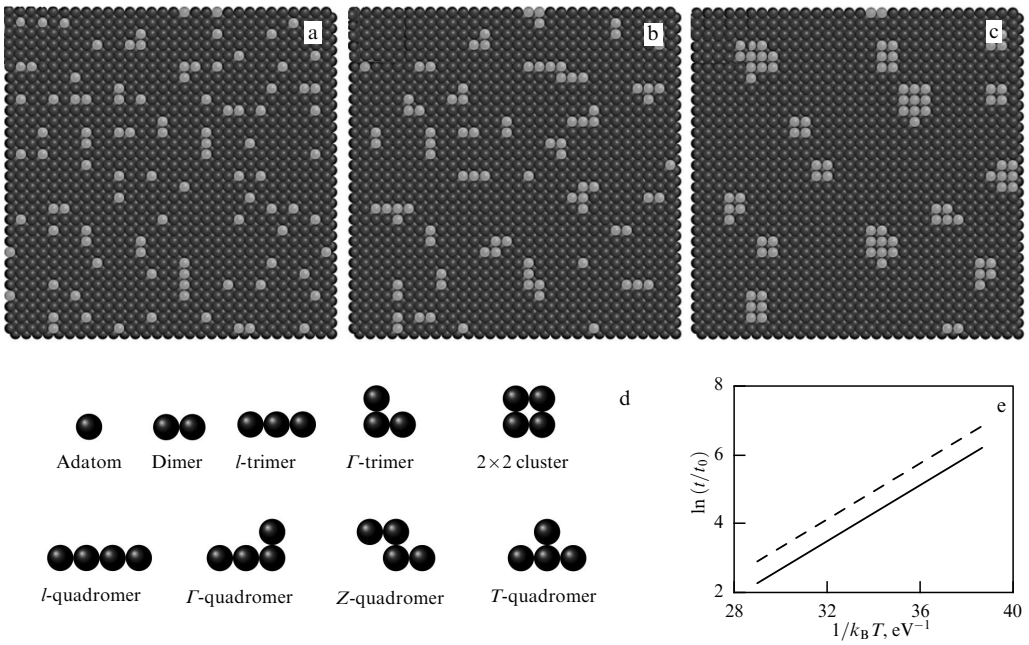

Figure 16. Three stages of nanostructure formation from Co atoms in first layer of Cu(001) surface. Images of same part of computing domain (top view) obtained using Monte Carlo simulation [134] at stages of (a) adatom diffusion, (b) formation of atomic chains, and (c) formation of compact clusters. Images were obtained at $T = 400$ K, $n_{Co} = 10\%$; dark balls denote Cu atoms, light balls denote Co atoms. (d) All possible nanostructures consisting of 1–4 Co atoms. (e) Dependence of times t_{12} (solid line) and t_{23} (dashed line) on reciprocal temperature.

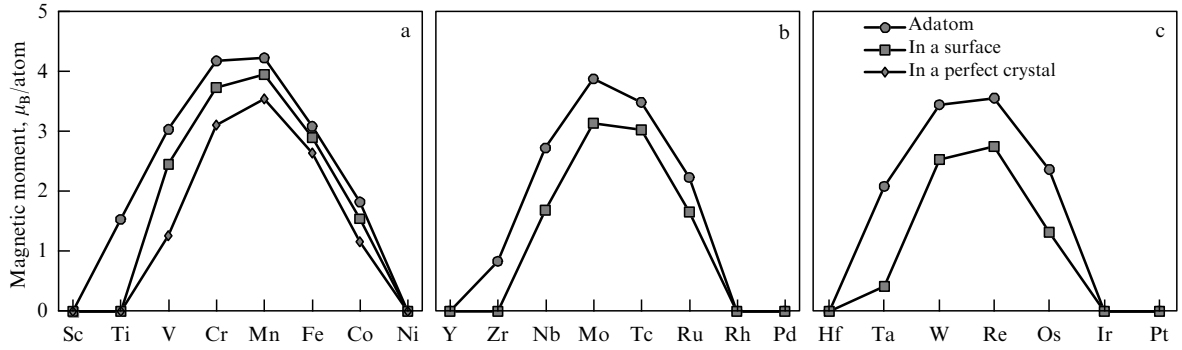

Figure 17. Magnetic moments (a) of 3d-metal atoms in bulk samples, on surface, and in first layer of Cu(001) surface, as well as of 4d- (b) and 5d-metal atoms (c) on surface and in first layer of Ag(001) surface [138].

structures of 1 to 4 atoms are shown in Fig. 16d. In the first layer of the surface of Cu(001), it is possible to form two types of trimers (l and Γ) and five types of quadromers (l, Γ, Z, and T, as well as compact 2×2 clusters).

We assume that the transition from the first stage to the second one occurs at time t_{12}, when the number of Co dimers becomes equal to the number of Co adatoms, and the transition from the second stage to the third occurs at time t_{23}, when the number of Co trimers becomes equal to the number of 2×2 clusters. In the temperature range of 300–400 K, the dependence of times t_{12} and t_{23} on the substrate temperature is well described by a simple exponential law (Fig. 16e),

$$t = t_0 \exp\left(\frac{E_A}{k_B T}\right), \tag{19}$$

where $E_A = 0.41$ eV is the activation energy of the formation of bound nanostructures from Co atoms, and t_0 is the time prefactor, which has an order of magnitude of $\sim 10^{-5\pm1}$ s for time t_{12} and $\sim 10^{-4\pm1}$ s for time t_{23}. Note that a change in the surface temperature in the range of 300–400 K significantly affects only the evolution rate in the system of embedded Co atoms. The qualitative picture of the bound nanostructure formation does not change. In Ref. [134], it was also shown that boundaries t_{12} and t_{23} between stages do not depend on the concentration of embedded Co atoms when it changes from 5% to 15%. Finally, note that considering the diffusion of dimers [135] in modeling leads to an acceleration of the process of nanostructure formation and a reduction in the duration of the second stage of nanostructure formation — the stage of formation of atomic chains. However, these chains turn out to be linear in most cases. Thus, by selecting the conditions for conducting the experiment, it is possible to achieve the formation of both atomic chains and compact clusters of Co atoms, which agrees with experimental results [45, 46].

Let us briefly discuss the self-arrangement of nanostructures from Fe atoms in the first layer of the Cu(001) surface [136, 137]. In general, the Co/Cu(001) and Fe/Cu(001) systems are very similar; however, the duration of the atomic chain formation stage in the Fe/Cu(001) system is reduced to almost zero. Keeping in mind some conventionality in defining the boundaries of stages t_{12} and t_{23}, we can say that, in the Fe/Cu(001) system, the stage of atomic chain formation is completely absent. Thus, the evolution of the Fe/Cu(001) system occurs in two stages: the diffusion of adatoms and the formation of compact clusters. In this case, hardly any linear chains of embedded Fe atoms are formed.

The results of calculations using the Green's function method showed in [138–142] that, on the surface of transition metals (Cu, Ag, Au, Pt, Pd, Ni, and Fe), the adatoms of 3d-metals are in a stable high-spin state. In this case, the magnetic moment of the atoms embedded in the first surface layer is greater than the magnetic moment of the same atoms in an ideal crystal, but smaller than on the surface (Fig. 17a). The change in the magnetic moment is associated with a change in the number of nearest neighbors of the atoms on the surface. Note that not all 3d-metal atoms in the first surface layer have a nonzero magnetic moment. For example, the magnetic moment of Ni atoms on the Cu(001) surface turns out to be zero due to the hybridization of the sp-electrons of the Ca(001) surface with the d-electrons of Ni.

More interesting behavior is exhibited by adatoms of 4d- and 5d-metals: in an ideal crystalline structure, their magnetic moments are zero, while the same atoms on the surface or in the first layer of transition metals may have nonzero magnetic moments. Figure 17b, c shows the magnetic moments of 4d- and 5d-metal adatoms on the surface and in the first layer of the Ag(001) surface [138], which appear due to a decrease in the number of nearest neighbors around the adatom. The adatoms with the largest magnetic moment are 4d-metals Mo and Tc and 5d-metals W and Re. The magnetic moments of the adatoms of Y, Rh, Pd, Hf, Ir, and Pt are zero.

The magnetic moments of adatoms depend on the substrate lattice constant. For example, the equilibrium lattice constant of silver is 12% greater than that of copper, which leads to an increase in the magnetic moment on the surface of Ag(001) compared to the surface of Cu(001). Calculating the densities of states and using the Stoner criterion, it can be concluded that the magnetic moments of adatoms on the surfaces of Au(001) and Ag(001) should be greater than on the surface of Cu(001) [138]. The results of comparing the magnetic moments of adatoms of 3d-, 4d-, and 5d-metals on the surfaces of Cu(001), Ag(001), Pd(001), and Pt(001) obtained by the KKR method in [143] confirm this conclusion. Moreover, the difference between the magnetic moments of 3d-metal adatoms on the Ag(001) and Cu(001) surfaces is not very large (not exceeding 30%). From this point of view, silver and copper surfaces are equally suitable for having nanoscale information carriers placed on them. Nevertheless, from the standpoint of mass production, it seems more reasonable to use copper substrates due to their lower cost.

The effect of mixing small clusters with a substrate on the magnetic properties of such clusters was studied in [141]. The KKR method was used to calculate the magnetic moments of atoms of 3×3 clusters of Ru, Rh, Os, Ir, Fe, and Co on the Ag(001) surface, various atoms of which were replaced by substrate atoms. It was found that various configurations of clusters with impurities have magnetic moments that differ significantly from the magnetic moments of ideal 3×3 clusters. Using Co, Rh, and Ir as examples, the effect of cluster size on its magnetic moment was examined [141]. It turned out that the dependence of the average value of the cluster atom's magnetic moment on its size is monotonic only for cobalt clusters. That is, the magnetic moment of a cobalt cluster on a metal substrate is proportional to the number of adatoms in the cluster and weakly depends on its geometric configuration. This fact makes cobalt clusters attractive from the point of view of their technical application as information bits.

In Refs [134, 144, 145], the magnetic properties of adatoms and small cobalt clusters embedded in the first layer of a Cu(001) surface were investigated. It was shown that the main difference from the case of small clusters on the Cu(001) surface [146] is the negative value of the magnetic anisotropy energy (MAE), i.e., the difference between the energies of the system when the magnetic moments of all atoms are directed parallel to the normal to the surface and perpendicular to it. Thus, it is energetically favorable for Co clusters in the first layer of the Cu(001) surface to have magnetization in the surface plane. Comparing the magnetic properties of the Co_9 cluster on the Cu(001) surface and in the first surface layer [144, 146], it can be concluded that embedding clusters in a copper substrate reduces the MAE and also leads to a more uniform distribution of orbital magnetic moments. For example, the MAE of the cluster corner atoms decreases by almost twofold when embedded. At the same time, the projections of the orbital magnetic moments on the surface plane do not change so significantly when embedding the cluster, and the spin magnetic moments of the cobalt atoms decrease by less than 2%.

Another interesting result of studies [134, 144, 145] is that the MAE of Co atoms in noncompact clusters is significantly higher than in compact Co_4 and Co_9 clusters. Similar results were obtained for nanostructures on Ag(001) and Au(001) surfaces [147, 148]. Moreover, on the Ag(001) surface, the MAE of Co atoms in the trimer is even higher than the MAE of a single Co adatom [147]. Thus, the highest MAE is characteristic of noncompact nanostructures.

Let us briefly consider the main differences between the magnetic properties of nanostructures of Co and Fe atoms in the first layer of the Cu(001) surface [28, 137, 145]. The spin magnetic moment of Fe atoms is approximately one and a half times greater than that of Co atoms. At the same time, the average MAE for nanostructures of Fe atoms is substantially smaller than the MAE for similar nanostructures of Co atoms [145]. Nanostructures of Fe and Co atoms have different directions of easy magnetization axes: if the easy magnetization axes of all Co nanostructures lie in the plane of the Cu(001) surface, then the easy magnetization axes of all Fe nanostructures (except for the adatom) are perpendicular to the surface. By comparing the results on self-arrangement and magnetic properties of nanostructures of Fe and Co atoms in the first layer of the Cu(001) surface, one can find the time evolution of the magnetic properties of the copper surface with atoms embedded in it [137].

The combination of self-arrangement and unusual magnetic properties makes nanostructures embedded in the first layer of the substrate possible candidates for future technical applications as information bits. It should be noted that obtaining ordered elements from embedded nanostructures is a more complex task than obtaining ordered nanostructures on the surface.

6. Clusters under surface

Impurity atoms located deeper than the first layer of the substrate surface are more difficult to detect experimentally than those on the surface or in the first layer of the surface. However, if the substrate is metallic, impurity atoms can be detected below the surface, since they scatter conduction electrons of the metal, and standing waves of electron density in the form of rings are observed on the surface [149, 150]. Figure 18a shows a diagram of such an experiment to detect Co atoms below the surface of Cu(001), and Fig. 18b–f shows STM images of the Cu(001) surface directly above the Co atom, obtained at a temperature of 6 K. The radius of the first ring of standing waves of electron density depends on the embedding depth of the impurity atom. Thus, all three coordinates of the impurity atom can be determined from the STM image of the surface.

When there is a small cluster under the surface, rather than a single impurity, it is possible to determine not only the depth of the cluster embedding but also its shape from the STM image of the surface [47–49]. As an example, let us consider the scheme of an experiment for detecting Ar clusters located under the Cu(001) surface (Fig. 19a). Electrons from the STM tip are injected into the substrate surface, reflected from the cluster and returned, forming standing waves of electron density on the copper surface. The length of the Bloch wave of the injected electron depends on the potential difference V between the surface and the STM tip; therefore, at different voltages V, the STM image of the surface directly above the cluster will look different (Fig. 19b–g). In this case, the normalized

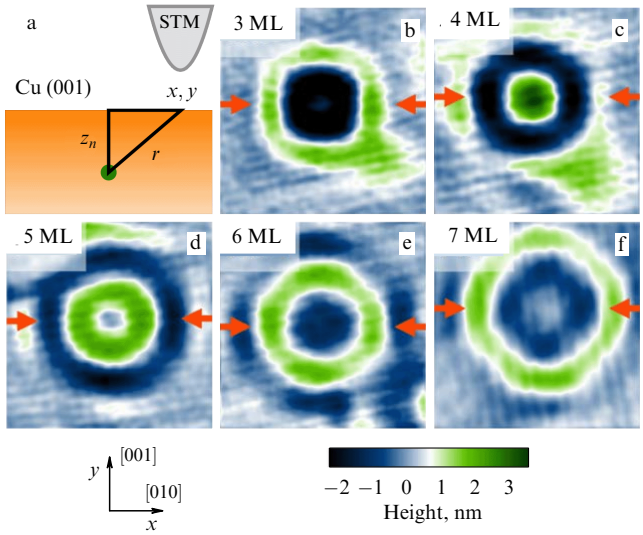

Figure 18. (a) Schematic diagram of experiment for detecting Co atoms under the surface. (b–f) STM images of Cu(001) surface with a Co atom embedded in it [149]. Co atom is located in 3rd, 4th, 5th, 6th, and 7th monolayer (ML) of surface, respectively. Surface is scanned at constant tunneling current of $I = 2$ nA and voltage of $V = 10$ mV.

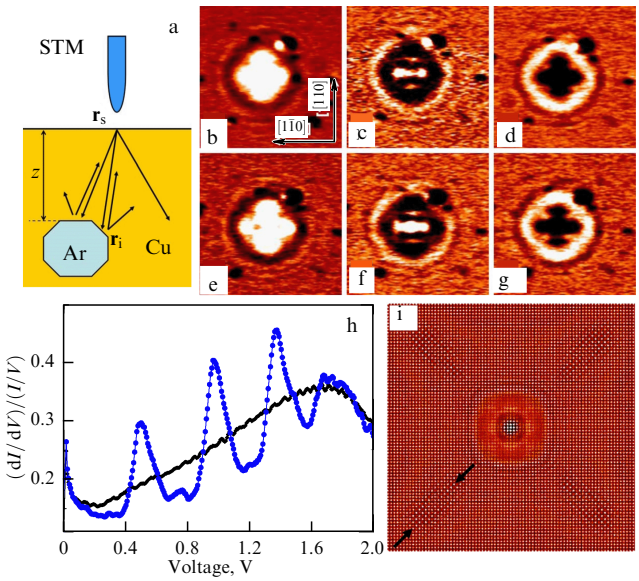

Figure 19. Observation of Ar clusters located under Cu(001) surface. (a) Schematic representation of electron propagation and reflection in a copper crystal. (b–g) STM images of Cu(001) surface directly above Ar cluster at a tunneling current of $I = 1.2$ nA and different voltages [47]: (b) 0.3 V, (c) 0.4 V, (d) 0.5 V, (e) 0.6 V, (f) 0.7 V, (g) 0.8 V. (h) Normalized differential conductivity $(dI/dV)/(I/V)$ of the surface areas above Ar cluster (blue dots) and far from the cluster (black dots). (i) Result of modeling surface conductivity near Ar cluster [48].

spectrum of differential conductivity $(dI/dV)/(I/V)$ of the surface above the Ar cluster has a pronounced oscillatory character (Fig. 19h). By measuring the period of such oscillations ΔE, one can find the depth z at which the Ar cluster is located, using the formula [47]

$$z = \frac{\pi}{\Delta E}\left|\frac{\partial E}{\partial \mathbf{k}}\right|, \qquad (20)$$

where $\mathbf{k}$ is the wave vector and $E(\mathbf{k})$ is the dispersion law of electrons moving in the [001] direction. In addition to the central spot, additional spots are also observed in the STM image, the appearance of which is associated with the reflection of electrons from the inclined faces and edges of the embedded cluster. Figure 19i shows a simulated STM image [48] of the Ar cluster, schematically shown in Fig. 19a. The black arrows in the figure indicate spots obtained as a result of the reflection of electrons from the inclined faces of the crystal. By constructing model images and comparing them with real STM images, the shape of embedded clusters can be determined [48, 49].

Let us discuss the mechanisms of diffusion of impurity atoms in the surface layers of Cu(001) using Co atoms as an example. As shown above, at a temperature of 300–400 K, the diffusion of Co atoms embedded in the first layer of the Cu(001) surface is activated. With an increase in temperature, Co atoms can embed themselves in deeper layers of copper. However, the diffusion of Co atoms in the bulk copper is activated only at temperatures above 800 K, which is associated with the sufficiently high activation energy of this process $E_{\text{bulk}} = 2.22$ eV [151]. At intermediate temperatures, Co atoms are embedded in the near-surface region of Cu(001) [152, 153]. Experimental studies [153, 154] have shown that Co atoms in the near-surface region at $T < 800$ K move only over the sites of the copper crystal lattice. Therefore, two different mechanisms of diffusion of Co atoms are possible. First, Co atoms can move due to the presence of vacancies in the near-surface region. Second, a diffusion mechanism is possible through cyclic permutation of Co and Cu atoms without the participation of vacancies. The simplest of such events are the permutation of two neighboring Co and Cu atoms and the cyclic permutation of three Co–Cu–Cu atoms in the (111) plane. To clarify the contribution of these mechanisms to the diffusion of Co atoms in the near-surface region, a diffusion model was proposed that considers all of the above events [154]. Moreover, the concentration of immersed Co atoms was assumed to be small enough so that the interaction between them could be ignored. In this case, it is sufficient to consider a one-dimensional model in which Co atoms move between the layers of the copper surface. In addition, the time of embedding a Co atom into the first layer of the Cu(001) surface at a temperature of $T = 650$ K is negligible compared to the time of executing the experiment, so it can be assumed that the Co atoms deposited on the Cu(001) surface immediately find themselves in the first layer of the copper surface.

In experiment [154], Co atoms were deposited on a Cu(001) surface in 30 seconds. The results of numerical integration of the diffusion equations for time $t = 30$ s (the moment of completion of cobalt deposition), $t = 10$ min, and $t = 55$ min are shown in Fig. 20a. The depth distribution of Co atoms, obtained experimentally under the same conditions, is shown in Fig. 20b. It is evident that, by the time the deposition is completed ($t = 30$ s), there are no Co atoms left in the first layer of the Cu(001) surface, in agreement with the experimental data. The rapid diffusion of Co atoms from the first to deeper layers of the Cu(001) surface at $T = 650$ K is due to relatively low diffusion barriers and activation energies for the diffusion of Co atoms in the upper layers of the surface ($E_A \approx 1.5$ eV). The depth distribution of Co atoms immediately after the end of the Co atom deposition has a maximum in the second layer of the Cu(001) surface. However, the diffusion of Co atoms in the near-surface region continues after the end of deposition. In a short period of time $\Delta t = 2.5$ s after the end of deposition, the concentrations of Co atoms in the second and third layers of Cu(001) become equal to each other (see the inset in Fig. 20a). And by the time $t = 10$ min, most of the Co atoms are in the third layer of the Cu(001) surface. Then, the number of atoms in the third layer begins to decrease because Co atoms diffuse into deeper near-surface layers. Comparing the depth distributions of Co atoms obtained theoretically (Fig. 20a) and experimentally (Fig. 20b), we see that the closest coincidence of the results corresponds to the time $t = 55$ min. An important result of Ref. [154] is the conclusion that the main mechanism of diffusion of Co atoms in the near-surface region of Cu(001) at temperatures close to 650 K is the vacancy mechanism.

Describing the growth of clusters under the surface at the atomic level is a much more complex task than studying the diffusion of single atoms. The fundamental complication of the problem is that, due to the mismatch of the lattice constants of copper and the cluster being formed, large mechanical stresses arise on the cluster surface, which can lead to the splitting of large clusters into smaller ones [155]. Obviously, under these conditions, it is necessary to consider the deformation of the crystal lattice near the cluster boundaries. This can be done, for example, within the framework of the nonlattice kinetic Monte Carlo method [105, 106, 156, 157]. However, as far as the authors know,

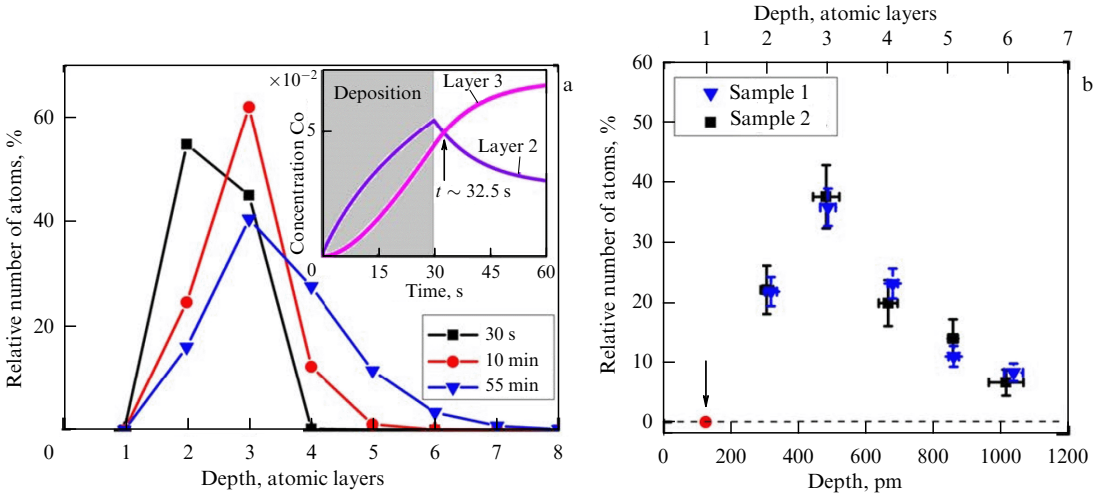

Figure 20. Distribution of Co atoms by depth of immersion in Cu(001) surface at temperature $T = 650$ K: (a) theoretical distributions at moments of time $t = 30$ s (end of Co atoms deposition), $t = 10$ min, and $t = 55$ min; (b) experimental distribution obtained from results of studying two samples [154]. Inset in Fig. a shows theoretical time dependences of concentrations of Co atoms in second and third layers.

such studies do not exist to date. Therefore, simple diffusion models are used to explain the growth of clusters under the surface at a qualitative level [158–160].

Successful detection of impurity atoms and atomic clusters hidden under the surface allows us to hope for their possible technical application, e.g., for storing information. However, to talk about possible technical applications, the process of formation of clusters embedded under the surface must be studied in detail. To date, both experimental and theoretical studies of related issues are far from being completed.

7. Conclusion

The review considered exotic nanostructures formed in bimetallic systems. It was shown that the formation of certain structures depends primarily on temperature.

At low temperatures of the order of several kelvins, superlattices consisting of individual atoms can form on the surface of metals. The possibility of forming such lattices is associated with Friedel oscillations of electron density on the close-packed surfaces of transition metals, which lead to oscillations of the potential energy of interaction of adatoms, depending on the distance between them. Depending on the ratio between the extremes of potential energy and thermal energy, adatoms can form either a two-dimensional crystal with a hexagonal lattice or some similarity to a liquid that does not have long-range order. The superlattice significantly affects the conductivity spectrum of the surface, which can be used in technology, for example, in low-temperature sensors.

At temperatures from 100 K to room temperature, flat dendrites can form in bimetallic systems. Depending on the surface and growth conditions, dendrites can have different symmetries. The fractal dimension of flat dendrites takes values from 5/3 to 2. Dendrites are formed both on flat areas of the surface and near steps. As the temperature increases, compact clusters are formed instead of dendrites on a flat surface, and finger-like protrusions are formed instead of dendrites near steps. The main patterns of formation of dendrites and finger-like protrusions were explained at the atomic level using the kinetic Monte Carlo method. To date, dendrites and finger-like protrusions have found practical application as catalysts for chemical reactions. The literature also discusses the issue of using such nanostructures for storing energy and information.

Magnetic nanostructures embedded in the surface layers of a nonmagnetic substrate seem promising from the point of view of information storage. Embedded nanostructures are formed at temperatures significantly higher than room temperature and are thermally more stable than structures of similar sizes formed on the surface. In addition, the formation of magnetic clusters in the surface layers of the substrate is promising for the creation of three-dimensional arrays for more compact storage of information.

The authors thank all their colleagues at Lomonosov Moscow State University. The authors express their gratitude to the Russian Science Foundation (grant 21-72-20034).

References

1. Chakraborty T, Pietilainen P *The Quantum Hall Effects: Integral and Fractional* (Springer Series in Solid-State Sciences, Vol. 85) (Berlin: Springer-Verlag, 1995)
2. Stormer H L *Rev. Mod. Phys.* **71** 875 (1999)
3. Datta S *Electronic Transport in Mesoscopic Systems* (Cambridge: Cambridge Univ. Press, 1995) https://doi.org/10.1017/CBO9780511805776
4. van Wees B J et al. *Phys. Rev. Lett.* **60** 848 (1988)
5. Katsnelson M I *Graphene: Carbon in Two Dimensions* (New York: Cambridge Univ. Press, 2012) https://doi.org/10.1017/CBO9781139031080
6. Novoselov K S et al. *Science* **306** 666 (2004)
7. Novoselov K S *Rev. Mod. Phys.* **83** 837 (2011); *Usp. Fiz. Nauk* **181** 1299 (2011)
8. Morozov S V, Novoselov K S, Geim A K *Phys. Usp.* **51** 744 (2008); *Usp. Fiz. Nauk* **178** 776 (2008)
9. Szacilowski K *Chem. Rev.* **108** 3481 (2008)
10. Žutić I, Fabian J, Das Sarma S *Rev. Mod. Phys.* **76** 323 (2004)
11. Enders A, Skomski R, Honolka J *J. Phys. Condens. Matter* **22** 433001 (2010)
12. Durkan C *Current at the Nanoscale* (Singapore: World Scientific, 2013) https://doi.org/10.1142/8371
13. Vajtai R (Ed.) *Springer Handbook of Nanomaterials* (New York: Springer, 2013) https://doi.org/10.1007/978-3-642-20595-8
14. Gogotsi Y (Ed.) *Nanomaterials Handbook* (Boca Raton, FL: CRC Press, 2017) https://doi.org/10.1201/9781315371795

15. Mustansar Hussain C (Ed.) *Handbook of Nanomaterials for Industrial Applications* (Amsterdam: Elsevier, 2018) https://doi.org/10.1016/C2016-0-04427-3
16. Kul'bachinskii V A *Fizika Nanostruktur* (Physics of Nanostructures) (Moscow: Fizmatlit, 2022)
17. Kolesnikov S V "Issledovanie samoorganizatsii nanostruktur na poverkhnosti medi" ("Study of self-arrangement of nanostructures on the copper surface"), PhD Thesis (Moscow: Lomonosov Moscow State University, 2010)
18. Wang J et al. *Mater. Today Phys.* **2** 6 (2017)
19. Kumar R et al. *Nano Res.* **12** 2655 (2019)
20. Chernozatonskii L A, Artyukh A A *Phys. Usp.* **61** 2 (2018); *Usp. Fiz. Nauk* **188** 3 (2018)
21. Ganatra R, Zhang Q *ACS Nano* **8** 4074 (2014)
22. Li X, Zhu H *J. Materiomics* **1** (1) 33 (2015)
23. Duong D L, Yun S J, Lee Y H *ACS Nano* **11** 11803 (2017)
24. Zhang D et al. *Nat. Rev. Mater.* **8** 25 (2023)
25. Klavsyuk A L, Saletsky A M *Phys. Usp.* **58** 933 (2015); *Usp. Fiz. Nauk* **185** 1009 (2015)
26. Rubio G, Agraït N, Vieira S *Phys. Rev. Lett.* **76** 2302 (1996)
27. Klavsyuk A L "Protsessy formirovaniya i svoistva metallicheskikh odnomernykh atomnykh struktur" ("Formation processes and properties of metallic one-dimensional atomic structures") Doct. Thesis (Moscow: Lomonosov Moscow State University, 2021)
28. Syromyatnikov A G et al. *Phys. Usp.* **64** 671 (2021); *Usp. Fiz. Nauk* **191** 705 (2021)
29. Choi D-J et al. *Rev. Mod. Phys.* **91** 041001 (2019)
30. Syromyatnikov A G "Teoreticheskoe issledovanie protsessov formirovaniya i strukturnykh svoistv metallicheskikh atomnykh provodov" ("Theoretical study of the processes of formation and structural properties of metallic atomic wires"), PhD Thesis (Moscow: Lomonosov Moscow State University, 2020)
31. Lu X, Akasaka T, Slanina Z *Handbook of Fullerene Science and Technology* (Singapore: Springer, 2022) https://doi.org/10.1007/978-981-16-8994-9
32. Dresselhaus M S, Dresselhaus G, Avouris P (Eds) *Carbon Nanotubes. Synthesis, Structure, Properties, and Applications* (Topics in Applied Physics, Vol. 80) (Berlin: Springer-Verlag, 2001) https://doi.org/10.1007/3-540-39947-X
33. Charlier J-C, Blase X, Roche S *Rev. Mod. Phys.* **79** 677 (2007)
34. Pei L Z, Wang S B, Fan C G *Recent Patents Nanotechnol.* **4** (1) 10 (2010) http://doi.org/10.2174/187221010790712138
35. Park M-H et al. *Angew. Chem. Int. Ed.* **50** 9647 (2011)
36. Bardi U *Rep. Prog. Phys.* **57** 939 (1994)
37. Loskutov A Yu, Mikhailov A S *Osnovy Teorii Slozhnykh Sistem* (Fundamentals of the Theory of Complex Systems) (Moscow–Izhevsk: Regulyarnaya i Khaoticheskaya Dinamika, Inst. Komp'yut. Issled., 2007)
38. Alexandrov D V, Galenko P K *Phys. Usp.* **57** 771 (2014); *Usp. Fiz. Nauk* **184** 833 (2014)
39. Farmer J D, Ott E, Yorke J A *Physica D* **7** 153 (1983)
40. Kolmogorov A N *Dokl. Akad. Nauk SSSR* **119** 861 (1958)
41. Brune H et al. *Surf. Sci.* **349** L115 (1996)
42. Negulyaev N N et al. *Phys. Rev. B* **77** 125437 (2008)
43. Lucci F R et al. *J. Phys. Chem. C* **118** 3015 (2014)
44. Lucci F R et al. *J. Phys. Chem. C* **119** 24351 (2015)
45. Kurnosikov O, Kohlhepp J T, de Jonge W J M *Europhys. Lett.* **64** 77 (2003)
46. van Gastel R et al. *Surf. Sci.* **605** 1956 (2011)
47. Kurnosikov O et al. *Phys. Rev. B* **77** 125429 (2008)
48. Kurnosikov O et al. *Phys. Rev. Lett.* **102** 066101 (2009)
49. Kurnosikov O, Swagten H J M, Koopmans B *Phys. Rev. Lett.* **106** 196803 (2011)
50. Braun O M, Medvedev V K *Sov. Phys. Usp.* **32** 328 (1989); *Usp. Fiz. Nauk* **157** 631 (1989)
51. Shockley W *Phys. Rev.* **56** 317 (1939)
52. Baranov A N "Fizicheskie svoistva adatomov i malykh klasterov na poverkhnosti metallov" ("Physical properties of adatoms and small clusters on the surface of metals"), PhD Thesis (Moscow: Lomonosov Moscow State University, 2002)
53. Smirnov A S "Nanostruktury, stabilizirovannye poverkhnostnymi sostoyaniyami, i ikh magnitnye svoistva: teoreticheskie issledovaniya" ("Nanostructures stabilized by surface states and their magnetic properties: theoretical studies"), PhD Thesis (Moscow: Lomonosov Moscow State University, 2009)
54. Park K-H et al. *Appl. Phys. Lett.* **75** 139 (1999)
55. Knorr N et al. *Phys. Rev. B* **65** 115420 (2002)
56. Stepanyuk V S et al. *Phys. Rev. B* **68** 205410 (2003)
57. Silly F et al. *Phys. Rev. Lett.* **92** 016101 (2004)
58. Crommie M F, Lutz C P, Eigler D M *Science* **262** 218 (1993)
59. Crommie M F, Lutz C P, Eigler D M *Nature* **363** 524 (1993)
60. Syromyatnikov A G, Klavsyuk A L, Saletsky A M *JETP Lett.* **100** 24 (2014); *Pis'ma Zh. Eksp. Teor. Fiz.* **100** 26 (2014)
61. Morgenstern K, Rieder K-H *New J. Phys.* **7** 139 (2005)
62. Tierney H L, Baber A E, Sykes E C H *J. Phys. Chem. C* **113** 7246 (2009)
63. Bardeen J *Phys. Rev. Lett.* **6** 57 (1961)
64. Tersoff J, Hamann D R *Phys. Rev. B* **31** 805 (1985)
65. Lau K H, Kohn W *Surf. Sci.* **75** 69 (1978)
66. Repp J et al. *Phys. Rev. Lett.* **85** 2981 (2000)
67. Hyldgaard P, Persson M *J. Phys. Condens. Matter* **12** L13 (2000)
68. Stepanyuk V S et al. *Phys. Rev. B* **70** 075414 (2004)
69. Ziegler M et al. *Phys. Rev. B* **79** 075401 (2009)
70. Ternes M et al. *Prog. Surf. Sci.* **85** (1) 1 (2010)
71. Negulyaev N N et al. *Phys. Rev. Lett.* **102** 246102 (2009)
72. Ziegler M et al. *Phys. Rev. B* **78** 245427 (2008)
73. Yokoyama T et al. *Phys. Rev. Lett.* **98** 206102 (2007)
74. Ternes M et al. *Phys. Rev. Lett.* **93** 146805 (2004)
75. Fernandez-Torrente I et al. *Phys. Rev. Lett.* **99** 176103 (2007)
76. von Hofe Th, Kröger J, Berndt R *Phys. Rev. B* **73** 245434 (2006)
77. Negulyaev N N et al. *Phys. Rev. B* **79** 195411 (2009)
78. Negulyaev N N et al. *Phys. Rev. B* **74** 035421 (2006)
79. Dong L, Gao Z, Lin N *Prog. Surf. Sci.* **91** 101 (2016)
80. Barth J V *Annu. Rev. Phys. Chem.* **58** 375 (2007)
81. Butova V V et al. *Russ. Chem. Rev.* **85** 280 (2016); *Usp. Khim.* **85** 280 (2016)
82. Ogura S et al. *Phys. Rev. B* **73** 125442 (2006)
83. Brodde A et al. *J. Vac. Sci. Technol. B* **9** 920 (1991)
84. Sibert E et al. *Surf. Sci.* **572** 115 (2004)
85. Wasniowska M et al. *Phys. Rev. B* **78** 035405 (2008)
86. Parschau M, Christmann K *Berichte Bunsengesellschaft phys. Chemie* **99** 1376 (1995)
87. Käsberger U, Jakob P *Surf. Sci.* **540** 76 (2003)
88. Bach Aaen A et al. *Surf. Sci.* **408** 43 (1998)
89. Hwang R Q et al. *Phys. Rev. Lett.* **67** 3279 (1991)
90. Röder H et al. *Phys. Rev. Lett.* **74** 3217 (1995)
91. Buchner F *STM Investigation of Molecular Architectures of Porphyrinoids on a* Ag(111) *Surface: Supramolecular Ordering, Electronic Properties and Reactivity* (Berlin: Springer-Verlag, 2010)
92. Meyer A et al. *Phys. Rev. B* **82** 085424 (2010)
93. Parschau M, Schlatterbeck D, Christmann K *Surf. Sci.* **376** 133 (1997)
94. Vicsek T *Fractal Growth Phenomena* (Singapore: World Scientific, 1992) https://doi.org/10.1142/1407
95. Witten T A (Jr.), Sander L M *Phys. Rev. Lett.* **47** 1400 (1981)
96. Langer J S *Rev. Mod. Phys.* **52** 1 (1980)
97. Witten T A, Sander L M *Phys. Rev. B* **27** 5686 (1983)
98. Niemeyer L, Pietronero L, Wiesmann H J *Phys. Rev. Lett.* **52** 1033 (1984)
99. Honda K, Toyoki H, Matsushita M *J. Phys. Soc. Jpn.* **55** 707 (1986)
100. Meakin P *Phys. Rev. A* **27** 604 (1983)
101. Matsushita M et al. *J. Phys. Soc. Jpn.* **55** 2618 (1986)
102. Voter A F *Phys. Rev. B* **34** 6819 (1986)
103. Fichthorn K A, Weinberg W H *J. Chem. Phys.* **95** 1090 (1991)
104. Trushin O et al. *Phys. Rev. B* **72** 115401 (2005)
105. Henkelman G, Jónsson H *J. Chem. Phys.* **115** 9657 (2001)
106. Kolesnikov S V et al. *Math. Models Comput. Simul.* **10** 564 (2018); *Matem. Modelirovanie* **30** (2) 48 (2018)
107. Soy E, Liang Z, Trenary M *J. Phys. Chem. C* **119** 24796 (2015)
108. Todoroki N et al. *Electrocatalysis* **7** 97 (2016)
109. Dokukin S A, Kolesnikov S V, Saletsky A M *Surf. Sci.* **689** 121464 (2019)
110. Zhang H et al. *J. Alloys Compd.* **698** 654 (2017)
111. Rashid Md H, Mandal T K *J. Phys. Chem. C* **111** 16750 (2007)
112. Yan W et al. *J. Energy Chem.* **64** 583 (2022)

113. Oura K et al. *Surface Science. An Introduction* (Berlin: Springer, 2003) https://doi.org/10.1007/978-3-662-05179-5
114. Woodruff D P (Ed.) *Surface Alloys and Alloy Surfaces* (The Chemical Physics of Solid Surfaces, Vol. 10) (Amsterdam: Elsevier, 2002)
115. Dastoor P C et al. *Surf. Sci.* **588** 101 (2005)
116. Canzian A, Mosca H O, Bozzolo G *Surf. Rev. Lett.* **11** 235 (2004)
117. Dokukin S A et al. *J. Alloys Compd.* **763** 719 (2018)
118. Dokukin S A, Kolesnikov S V, Saletsky A M *Comput. Mater. Sci.* **155** 209 (2018)
119. Dokukin S A, Kolesnikov S V, Saletsky A M *J. Exp. Theor. Phys.* **135** 671 (2022); *Zh. Eksp. Teor. Fiz.* **162** 686 (2022)
120. Dokukin S A, Kolesnikov S V, Saletsky A M *Eur. Phys. J. B* **95** 161 (2022)
121. Ustinovshchikov Yu I *Phys. Usp.* **63** 668 (2020); *Usp. Fiz. Nauk* **190** 715 (2020)
122. Grant M L et al. *Phys. Rev. Lett.* **86** 4588 (2001)
123. van Gastel R et al. *Surf. Sci.* **521** 10 (2002)
124. Schmid A K et al. *Phys. Rev. Lett.* **77** 2977 (1996)
125. Flores T, Junghans S, Wuttig M *Surf. Sci.* **371** 1 (1997)
126. Horch S et al. *Nature* **398** 134 (1999)
127. Varotsos P A, Alexopoulos K D (Eds) *Thermodynamics of Point Defects and Their Relation with Bulk Properties* (Defects in Solids, Vol. 14) (Amsterdam: North-Holland, 1986)
128. Korzhavyi P A et al. *Phys. Rev. B* **59** 11693 (1999)
129. Polatoglou H M, Methfessel M, Scheffler M *Phys. Rev. B* **48** 1877 (1993)
130. Devyatko Yu N, Rogozhkin S V, Fadeev A V *Phys. Rev. B* **63** 193401 (2001)
131. McCarty K F, Nobel J A, Bartelt N C *Nature* **412** 622 (2001)
132. Hoshino T et al. *Phys. Rev. B* **47** 5106 (1993)
133. Kolesnikov S V, Klavsyuk A L, Saletsky A M *Phys. Rev. B* **79** 115433 (2009)
134. Kolesnikov S V, Klavsyuk A L, Saletsky A M *Surf. Sci.* **612** 48 (2013)
135. Kolesnikov S V, Klavsyuk A L, Saletsky A M *Eur. Phys. J. B* **86** 399 (2013)
136. Kolesnikov S V *JETP Lett.* **99** 286 (2014); *Pis'ma Zh. Eksp. Teor. Fiz.* **99** 329 (2014)
137. Kolesnikov S V, Klavsyuk A L, Saletsky A M *J. Exp. Theor. Phys.* **121** 616 (2015); *Zh. Eksp. Teor. Fiz.* **148** 706 (2015)
138. Lang P et al. *Solid State Commun.* **92** 755 (1994)
139. Stepanyuk V S et al. *J. Magn. Magn. Mater.* **165** 272 (1997)
140. Stepanyuk V S et al. *Phys. Rev. B* **54** 14121 (1996)
141. Stepanyuk V S et al. *Phys. Rev. B* **59** 1681 (1999)
142. Wildberger K et al. *Phys. Rev. Lett.* **75** 509 (1995)
143. Stepanyuk V S et al. *Phys. Rev. B* **53** 2121 (1996)
144. Pick Š et al. *Phys. Rev. B* **70** 224419 (2004)
145. Klavsyuk A L, Kolesnikov S V, Saletsky A M *JETP Lett.* **99** 646 (2014); *Pis'ma Zh. Eksp. Teor. Fiz.* **99** 750 (2014)
146. Pick Š et al. *Phys. Rev. B* **68** 104410 (2003)
147. Lazarovits B, Szunyogh L, Weinberger P *Phys. Rev. B* **65** 104441 (2002)
148. Cabria I et al. *Phys. Rev. B* **65** 054414 (2002)
149. Prüser H et al. *Phys. Rev. Lett.* **108** 166604 (2012)
150. Weismann A et al. *Science* **323** 1190 (2009)
151. Döhl R, Macht M-P, Naundorf V *Phys. Status Solidi A* **86** 603 (1984)
152. Ramsperger U et al. *Phys. Rev. B* **53** 8001 (1996)
153. Siahaan T et al. *Phys. Rev. B* **90** 165419 (2014)
154. Siahaan T et al. *Phys. Rev. B* **94** 195435 (2016)
155. Lubov M N, Trushin Yu V *Tech. Phys. Lett.* **41** 102 (2015); *Pis'ma Zh. Tekh. Fiz.* **41** 104 (2015)
156. Henkelman G, Jónsson H *Phys. Rev. Lett.* **90** 116101 (2003)
157. Xu H, Osetsky Yu N, Stoller R E *Phys. Rev. B* **84** 132103 (2011)
158. Kurnosikov O et al. *Phys. Rev. B* **84** 054109 (2011)
159. Kulikov D V et al. *Appl. Surf. Sci.* **267** 128 (2013)
160. Kulikov D V et al. *Tech. Phys. Lett.* **35** 57 (2009); *Pis'ma Zh. Tekh. Fiz.* **35** (2) 8 (2009)